X-ray diffraction from levitated liquids

2000 J. Phys.: Condens. Matter 12 R145

(http://iopscience.iop.org/0953-8984/12/12/201)

J. Phys.: Condens. Matter **12** (2000) R145–R176. Printed in the UK PII: S0953-8984(00)03633-X

REVIEW ARTICLE

X-ray diffraction from levitated liquids

Shankar Krishnan† and David L Price‡

† Containerless Research Inc., Evanston, IL 60201, USA
‡ Argonne National Laboratory, Argonne, IL 60439, USA

Received 8 November 1999, in final form 3 February 2000

Abstract. The ability of containerless techniques to access very high liquid temperatures, maintain specimen purity, enable control of specimen chemistry and access the supercooled state has created new opportunities to study high-temperature liquids with a very high degree of control. Recently, these have been combined with x-ray diffraction at synchrotron sources to provide structural information not previously available. This article reviews and summarizes recent results obtained from x-ray diffraction on levitated liquid materials in both the normal and supercooled states. In particular, it addresses the effects of supercooling on the short-range structure, including interatomic distances and coordinations, of several high-temperature molten oxides, semiconductors and metallic materials. The properties of these liquids are discussed in the context of available molecular dynamics simulations and thermophysical property data.

1. Introduction

Structural studies on contained materials at high-temperature have to contend with two distinct problems: (i) container interactions and contamination, and (ii) the effects of the container walls on the structural measurements. Because most structural measurements require extended durations, on the order of several minutes to hours, there have been few attempts to study liquids above 2000 K. The situation has changed dramatically with the recent efforts to combine containerless methods with x-ray techniques. These have also made it possible to investigate the supercooled (metastable) liquid state by eliminating container-induced heterogenous nucleation. This article reviews the early results obtained in the last four years in studying levitated liquids by x-ray diffraction.

There has been a resurgence of interest in the structural properties of supercooled liquids in light of the possible occurrence of first-order phase transitions and the nature of the liquid structure prior to nucleation. For example, first-order liquid–liquid phase transitions have been observed in supercooled yttria–alumina mixtures [1] and predicted to occur in tetrahedrally bonded systems like Si and Ge [2]. Other interesting phenomena include the reported occurrence of magnetic ordering in hypercooled liquid Co–Pd alloys [3], the existence of metastable miscibility gaps [4] and liquids exhibiting fragile behaviour upon supercooling [5]. However, attempts to establish a correlation between structural changes and the observed property variations with supercooling have met with limited success. Improvements to diffraction techniques are needed to establish such correlations and to develop theoretical models to explain the observed behaviour in the supercooled liquid state.

A variety of containerless techniques are available to the researcher to study high-temperature liquids in the normal and supercooled states [6]. The most widely practiced containerless techniques are: electromagnetic levitation (EML) [7], conical nozzle levitation

(CNL) [8, 9], electrostatic levitation (ESL) [10] and aero-acoustic levitation (AAL) [11]. EML and CNL have been the primary techniques employed in conjunction with x-ray measurements, while the complexity of ESL and AAL hardware has limited their use for structural studies thus far. EML can only be used with metallic specimens: specimens $>$ 3 mm in diameter can be stably positioned between two sets of oppositely wound coils. A radiofrequency (100–500 kHz) source is used to both levitate and inductively heat the specimens. CNL uses aerodynamic flow through a divergent nozzle. The specimen, which can be an insulator or a metal, is stably positioned within the nozzle. Laser heating is then used to raise the temperature to the required level. Further details on the use of containerless techniques to study reactive materials can be found in a recent review [6].

This article provides an in-depth review of x-ray measurements of the atomic structure of levitated liquids. It draws on work performed over the last four years, principally by our research groups. Structural results have been published on levitated liquid silicon [12], Al_2O_3 [13], boron [14], Y_2O_3 [15, 16], $Co_{80}Pd_{20}$ [17] and YAG [18] in both the normal and supercooled states. This article also includes some x-ray results on levitated liquids given here for the first time. While it focuses on x-ray scattering studies of levitated liquids, it is noted that there has been extensive use of the EXAFS technique to study levitated liquids by the research groups in France and Germany [19–25].

The following section describes some of the experimental techniques associated with CNL, the primary technique employed by our research group [26] and that in Orleans, France [19–21]. The group in Koln, Germany [22–25] has used the EML technique for EXAFS studies on levitated liquids. Details of their experimental methods can be found in two recent papers [24, 25].

2. Experimental methods

The integration of a levitation device with an x-ray goniometer or detector system requires a coincidence of the specimen and detector centres. This was achieved by attaching the levitation system directly to the x-ray goniometer (typically a Huber six-circle goniometer). Because most goniometers are set up for operation in a vertical plane, it was necessary to ensure complete access to the specimen in the vertical plane above the sample. Such access is easily afforded by the CNL system, but not possible in the EML system due to the presence of levitation coils. The sections below describe the various parts of the levitation and x-ray systems, and data analysis methods.

2.1. Description of the apparatus

The CNL system, integrated with a Huber, six-circle, x-ray diffractometer at a typical beamline is schematically illustrated in figure 1. A photograph of the CNL system, integrated with the six-circle goniometer at beamline X-25 at the National Synchrotron Light Source, is shown in figure 2. The two figures show all of the key components including the two pyrometers (P1, P2), two video cameras (V1, V2) and video microscope (VM3), curved Be window (W), Huber goniometer (H), and x-ray detector (X), shown at the very top of the photograph. The levitation chamber is located at the centre of the Huber goniometer. The heating laser was inclined at 15° with respect to the normal to avoid physical interference with the x-ray detector.

The nozzle and plenum chamber assembly were supported on three tubes that connected to three flexible bellow feedthroughs. Two of these flow tubes circulated water for nozzle cooling, while the third flow tube supplied the levitation gas that fed into the nozzle's plenum chamber. The CNL system was enclosed in an environmentally controlled chamber with suitable ports

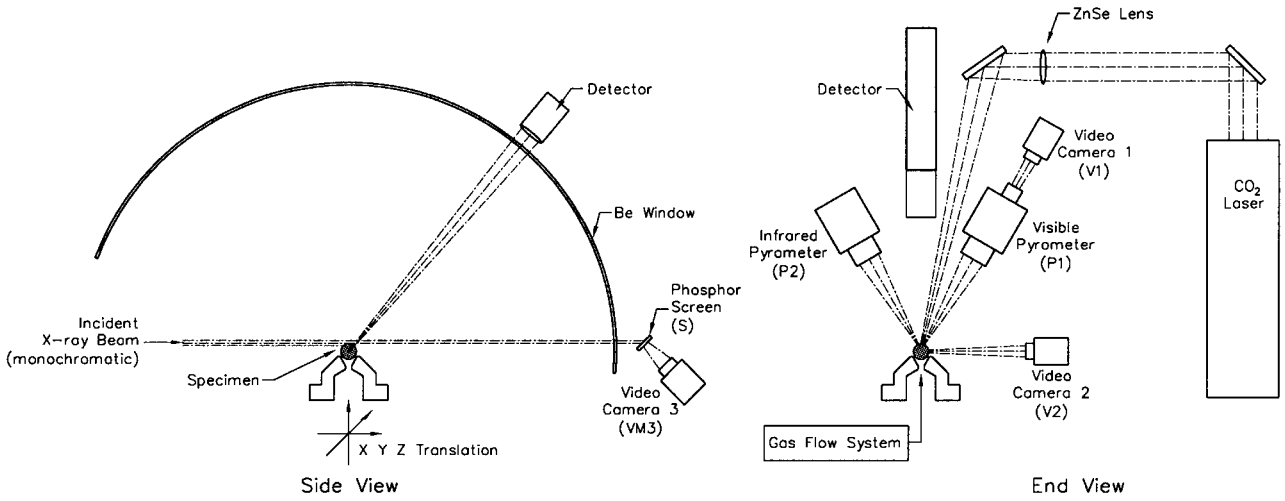

Figure 1. Schematic diagram of apparatus used for measurements of liquid structure showing the levitated specimen in the conical nozzle, x-ray diffraction geometry, heating laser, pyrometry, video imaging and phosphor screen. Key components are labelled and discussed in the text.

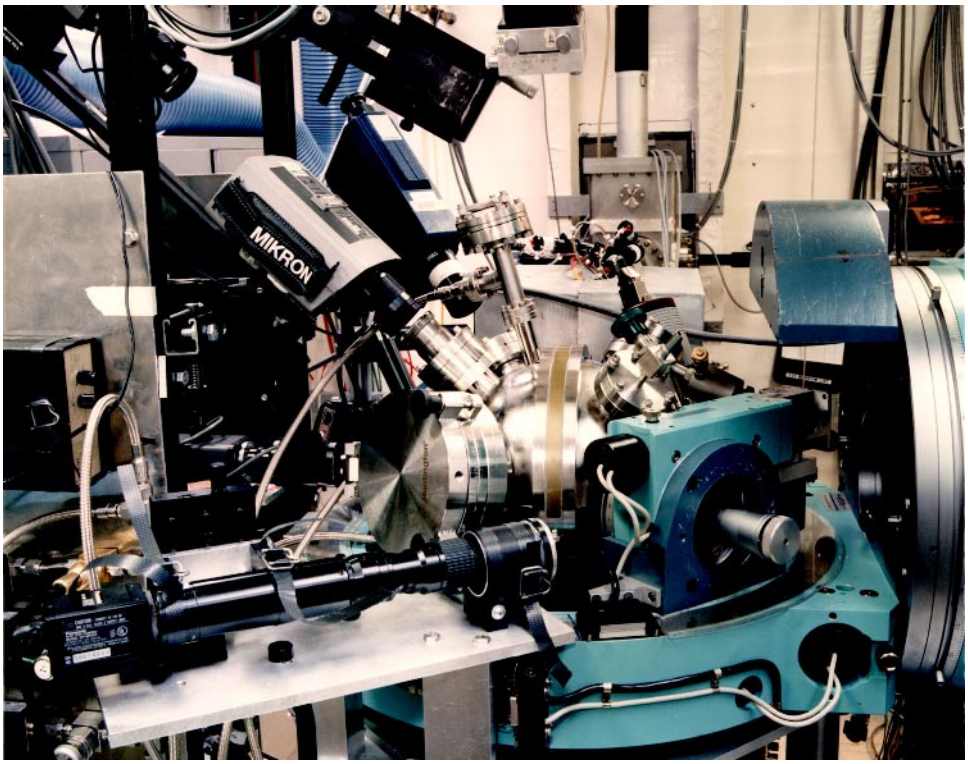

Figure 2. Photograph of the levitation apparatus integrated with a Huber six-circle x-ray diffractometer at beamline X-25 at the National Synchrotron Light Source. The two pyrometers and heating laser optics are on the left. The curved Be window is in the centre of the photograph. The video microscope is in the lower centre of the photograph.

for laser heating, pyrometry, sample injection and retrieval, and pressure measurements. The upper part of the chamber was a 9 inch diameter sphere. Two beryllium windows were included in this section; the first was a small window for the incident x-ray beam which was placed at the end of a radial tube port. The second window was curved, approximately 8 mm wide and 0.127 mm thick, and subtended approximately 120° around the nominal specimen position at the centre of the chamber. This window extended to about 5° below the normal levitation height of the specimen, enabling transmission of the direct x-ray beam.

The gas flow to the CNL was regulated using electronically controlled mass flow controllers. The chamber was connected to a vacuum system that allowed for evacuation to about 10^{-5} bar (1 bar $= 10^5$ Pa). An exhaust throttle valve, placed between the pump and the chamber, allowed control of the chamber pressure in the range 0.1–0.8 bar during levitation. The specimens were heated with the aid of a 270 watt CO_2 laser (Synrad model 60-2). Temperature measurements were obtained with two pyrometers whose operating wavelengths were 0.65 and 1–2.5 μm, respectively. Precise sample positioning was achieved by moving the nozzle assembly with a three-axis motorized translator, and using a phosphor screen to observe the shadow of the specimen in the x-ray beam that passed over the very top of the specimen. Specimen materials could be levitated, heated, melted and positioned stably for up to 3 hours, sufficient for the x-ray diffraction studies.

The CNL technique is based upon the previous work of Winborne *et al* [8] and Coutures *et al* [9], and on recent developments reported by Weber and Nordine [27] in which specimens

were stably levitated by gas flow in a divergent nozzle and laser heated to temperatures in excess of 2500 K.

The condition for levitation is derived from the momentum conservation applied to a control volume that contains the specimen:

$$\int [\rho u^2 + p]\,\mathrm{d}A = Mg. \tag{1}$$

Here, ρ, u and p are the gas density, vertical gas flow velocity and gas pressure, and Mg is the specimen weight. The integral is performed over the control volume surface, A.

Free-jet and conical nozzle levitation differ in the magnitude of the two components on the left side of equation (1). Stable free jet levitation occurs when the gas flow is sufficient to form a free jet with a momentum flow rate equal to about twice the specimen weight. Stable levitation in a conical nozzle occurs when the momentum flow is less than the specimen weight, and the levitation results mainly from pressure differences over the specimen surface. The pressure differences are a small fraction of the total pressure; for example, a 3 mm diameter sphere of liquid aluminium oxide is levitated when the pressure difference across the sample is approximately 0.001 bar, or about 0.1% of the total pressure at one atmosphere.

In most experiments, the chamber was initially pumped down to low pressure and then purged for short durations with gas flow. The system could then be filled with argon. A full-throat, servo-controlled throttle valve located between the chamber and the pump maintained the chamber at any desired pressure between 0.1 and 0.7 bar over the range of gas flow typically employed for levitation and gas purge. The typical flow rates used for metals at 0.4 bar varied from 150 to 600 standard cm^3 per minute. For all of the experiments on metals, UHP argon was employed as the levitation gas. For selected experiments on oxide ceramics, air, pure oxygen or nitrogen was used as the levitation gas.

A Synrad model 60-2, 270 watt cw CO_2 laser was used for specimen heating. The heating laser beam was tilted with respect to the vertical plane by approximately 15° to avoid interference with the motion of the x-ray detector. The heating laser beam was directed at the specimen with two laser mirrors and a ZnSe lens placed between the mirrors. Two independent laser power controllers, one located inside the x-ray hutch, and one located outside the beamline hutch in the electronics rack, were used to independently control the laser power. The operation of the lasers was interlocked with the x-ray hutch door for safety.

Two automatic optical pyrometers were simultaneously employed in the CNL apparatus: one, a Mikron model M90V, operating at 0.65 μm and the other, a Heimann model KT19.99 operating in the 1–2.5 μm bandpass. The pyrometers were oriented at 45° on either side of the vertical plane. Temperature measurements were obtained at a point on the surface of the specimen closest to the illumination point of the x-ray beam. The minimum spot sizes were about 1 mm for the visible wavelength pyrometer and about 1.9 mm for the infrared pyrometer. Specimen temperatures were stable within about ±20 K over the duration of the diffraction scans. This variation in specimen temperature was not considered severe since most of the structural results show only moderate temperature dependence.

Pyrometry or radiometry is essential for temperature measurements in containerless experimentation. The major drawback is the need for spectral emissivity data that are required to derive true temperatures from radiance measurements. Emissivity results previously published in the literature for liquid Al_2O_3 [28], liquid Si [29], liquid Ni [30, 31] were used to correct the radiance temperatures. For other materials emissivity values were selected based on the radiance temperatures observed at the melting point combined with the known melting or liquidus temperature and using the assumption that the spectral emissivity was independent of temperature.

The radiance (or apparent) temperature, T_a, is related to the true temperature, T, through Wien's law, which is accurate to better than 1% when the product λT is less than 3000 μm K. The relationship between true and radiance temperatures is then given by:

$$\frac{1}{T} - \frac{1}{T_a} = \frac{\lambda}{C_2} \ln(\varepsilon_\lambda). \tag{2}$$

In equation (2), ε_λ is the spectral emissivity of the material at the pyrometer effective wavelength, λ, and $C_2 = 1.4388$ cm K is Planck's second radiation constant. The effective wavelength of the visible pyrometer was 0.65 μm. The infrared pyrometer had a bandpass of 1–2.5 μm, and this pyrometer was primarily used for low-temperature measurements and for diagnostic purposes. The visible pyrometer also employed a pair of close-focusing lenses which had an effective transmittance of 92%. In addition, a 92% window transmission correction was applied to the visible pyrometer radiance temperature and a correction for 91% transmission by the sapphire window was used in conjunction with the Heimann pyrometer. Window transmission values were experimentally determined in separate experiments. The absolute accuracy of radiance temperature measurements is estimated at ± 4 K at 2000 K based on all the uncertainties including window correction, pyrometer calibrations and measurement errors.

The absolute accuracy of radiance temperature measurements was verified in experiments on liquid nickel, whose melting temperature is reported to be 1729 ± 4 K [32]. In the CNL experiments, we obtained a radiance temperature of 1599 ± 3 K (at an effective wavelength of 0.65 μm) at the melting point of nickel, after window and lens transmission corrections. Using the recently measured emissivity of 0.362 [30, 31] for liquid Ni, a true melting temperature of 1726 ± 4 K was calculated, in good agreement with the results of [32].

One of the drawbacks of the CNL method is that specimens have temperature gradients between the laser-beam-heated top of the specimen and the bottom of the specimen where the cold levitation gas first impinges. Based on observations with the optical pyrometer and the observed maximum undercooling for well known materials, this difference was estimated to be about 25 K for liquid metals and on the order of 50–75 K for liquid oxides due to their reduced thermal conductivities. The advantage of x-ray diffraction in this context is that the scattering takes place from the region of the sample whose temperature is measured by pyrometry. Temperature gradients become more serious, however, for neutron diffraction and NMR or when the x-ray energy becomes sufficiently high to penetrate the interior of the sample.

2.2. X-ray system and data analysis

While a number of x-ray techniques may be employed for structural investigations such as total x-ray scattering, anomalous x-ray scattering and EXAFS, the only technique employed by our research groups has been total x-ray scattering. In particular, our approach has employed monochromatic x-rays combined with a fixed detector scanned over an angular range for measurements of the total structure factor, $S(Q)$. While this is a simple approach, it requires a high degree of sample stability over an extended duration, which was possible with the CNL system. Alternative approaches such as the use of a white beam combined with an energy dispersive detector at a fixed scattering angle should also be possible on levitated liquids. Use of a white beam source on levitated specimens is complicated by the spherical specimen shape, the x-ray form factors, and the typical white beam energy profile such that accurate low- and high-Q results require measurements at multiple scattering angles.

The results presented in this article were obtained from x-ray experiments performed at three beamlines, X-6B and X-25 of the National Synchrotron Light Source at Brookhaven National Laboratory, and 12-BM-B of the Advanced Photon Source at Argonne National Laboratory.

Scattered x-rays were recorded in a solid-state detector with 300 eV resolution over a 2θ angular range of 5–110° with an angular resolution of 0.1°. Incident x-ray beam energies were in the range of 6–21 keV. Diffraction data were obtained over a scattering vector ($Q = 4\pi \sin(\theta)/\lambda$) range between 0.8 to 15 Å^{-1} depending on the experiment. The measured intensity, $I(2\theta, E)$, corrected for dead time, detector efficiency and air scattering, is:

$$I(2\theta, E) = I_p(E)[A(2\theta, E, E')P(2\theta)I_{coh}(Q) + I_{MS}^{coh} + A(2\theta, E, E')I_{inc}(Q') + I_{MS}^{inc}] \tag{3}$$

where

- $I_p(E)$ = intensity of the incident beam
- $I_*(Q)$ = the coherent or incoherent scattering intensity
- $A(2\theta, E, E')$ = attenuation coefficient
- I_{*MS} = coherent or incoherent multiple scattering
- $P(2\theta, E)$ = polarization factor
- $E' = E/(1 + 0.003\,92E\sin^2(\theta))$
- $Q = 1.014E\sin(\theta)$, where Q is measured in Å^{-1} and E in keV
- $Q' = Q^*(1 - 0.001\,96E\sin^2(\theta))$.

The correction procedure employed a Monte Carlo simulation of the experimental geometry that was iterated against the measured data. The corrections were implemented through a two-stage refinement procedure: the first stage refined instrumental parameters, including photon density profile and detector efficiency derived from a statistical average of all the data sets obtained in the experimental run cycle, and specimen parameters including sample position in the beam, sample radius and density. In the second stage, individual runs were analysed using fixed instrumental and variable sample parameters. Form factors were obtained from Baro *et al* [33]; the temperature dependence of the form factors were obtained from [34]. In some cases, the form factors were assumed to be temperature independent.

The coherent scattered intensity, $I_{coh}(Q)$, is related to the x-ray weighted average structure factor, $S(Q)$, through the well known relationship:

$$S(Q) = \frac{(I_{coh}(Q) - \langle|f(Q)|^2\rangle)}{|\langle f(Q)\rangle|^2} + 1 \tag{4}$$

where $\langle f(Q)\rangle$ and $\langle f(Q)\rangle^2$ are the mean and mean squared scattering amplitudes. The duration of a single scan over a range of Q values was typically 10–15 minutes. The procedure was to obtain several sets of scattered x-ray data for each temperature and average the $S(Q)$ values. From $S(Q)$, the pair correlation function, $G(r)$, is given by:

$$G(r) - 1 = \frac{1}{2\pi^2\rho_a}\int_0^{Q_{max}} Q(S(Q) - 1)\frac{\sin(Qr)}{r}\mathrm{d}Q \tag{5}$$

where ρ_a is the number of atoms per unit volume. Because of the limited Q range of the x-ray data, the maximum entropy criterion [35] has been used in the work reported here, where $G(r)$ is constrained to unity at large r. Values of the number density, ρ_a, were either estimated or obtained from literature data for the different materials. It is noted that for cases where the number density was estimated, errors in the number density would lead to proportional errors in the derived coordination numbers, but would not affect the peak positions in the $G(r)$ to a first approximation.

On the basis of the observed scattering, estimates of coordination number can be obtained from the $G(r)$ using the relation:

$$4\pi\rho_a\int_{r_1}^{r_2} G(r)r^2\,\mathrm{d}r = \frac{\Sigma}{ab}\frac{f_a f_b}{|\langle f\rangle|^2}X_a C_a(b) \tag{6}$$

where f_a and f_b are the scattering amplitudes of species a and b, X_a is the concentration of element a, $C_a(b)$ is the number of b atoms in a coordination shell about an a atom and r_1 and r_2 are the integration limits of the peak in $G(r)$.

3. Experimental results

The following sections review the structural properties of a range of high-temperature liquids studied. Specific details of the experiments, including x-ray energy ranges, mass loss data, correction procedures, number density values and other material specific attributes may be found in the specific publications [12–18]. This section also includes results obtained by various groups from MD simulations for the various materials.

The experimental results and discussion of the results are presented in three categories: oxide melts, silicon and boron (both of which undergo a change in their electronic structure upon melting) and metallic liquids. In each case, we present experimental structure factors, $S(Q)$, and pair correlation functions, $G(r)$, coordination numbers, nearest-neighbour distances etc. The structural results are compared with literature data and MD simulations for cases where such data are available. The structural results and their implications are discussed for each material based on available thermophysical and electronic property data.

3.1. Structures of high-temperature oxide melts

In this section, we describe the properties of two technologically important high-temperature oxide melts, aluminium oxide [13], and yttrium oxide [15, 16] that were investigated by a combination of levitation and x-ray techniques. The readers are alerted to some very recent work on yttrium aluminium garnet (62.5 mol% aluminium oxide and 32.5 mol% yttrium oxide) [18] that describes the properties of a mixture of yttrium and aluminium oxides.

Interest in the structural properties of liquid yttrium and aluminium oxide arises from the fact that these materials are widely used in the high temperature ceramics field. Alumina is one of the most widely used ceramic materials in refractory applications. Some forms of alumina such as sapphire are extensively used in optical and structural applications. The binary mixtures of yttria and alumina produce some technologically important phases such as YAG (yttrium aluminium garnet, $Y_3Al_5O_{12}$), YAP (yttrium aluminium perovskite, $YAlO_3$), and YAM (yttrium aluminium monoclinic, $Y_4Al_2O_9$).

3.1.1. Liquid aluminium oxide. The stable solid phase, α-aluminium oxide exhibits the corundum structure with Al atoms in octahedral sites surrounded by six oxygen neighbours at a distance of 1.91 Å. The metastable phase γ-Al_2O_3, is described by a defect spinel structure in which the Al coordination varies from three to five [36], with tetrahedral Al^{3+} predominating. The bonding in the liquid has been investigated extensively by Coutures *et al* [37] and Massiot *et al* [9] by ^{27}Al magic-angle spinning (MAS) NMR spectroscopy on liquid Al_2O_3. These studies inferred that the liquid consists of predominantly four-coordinated Al^{3+} with an average coordination of 4.5 ± 1.

Measurements on the liquid were performed at a photon energy in the range 6–9.5 keV. The structure factor $S(Q)$ for liquid Al_2O_3 is shown in figure 3 at specimen temperatures of 2223 and 2663 K [13], 104 K below and 336 K above the equilibrium melting point of 2327 K. Anomalies in $S(Q)$ at very low Q values may be ignored as these arise from inexact subtraction of the air scatter. The two prominent peaks in $S(Q)$ are at 2.05 and at 4.50 Å^{-1}. The pair correlation function, $G(r)$, is plotted in figure 4 for liquid Al_2O_3 at the same two temperatures. The $G(r)$ plot shows a strong peak at 1.76 Å, a second peak at 3.08 Å, and a third peak at

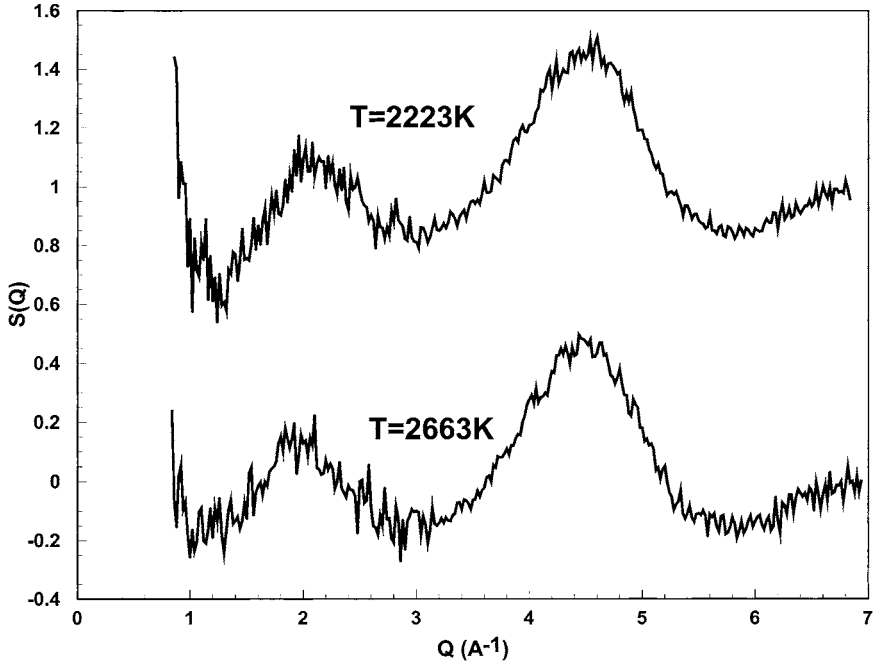

Figure 3. Structure factor, $S(Q)$ for liquid Al_2O_3 at 2223 K (upper curve) and at 2663 K (lower curve). The $S(Q)$ values for the lower curve have been shifted down by 1 for clarity.

4.25 Å. For the supercooled liquid, higher correlations are observed at distances up to 7 Å, which are less evident in the normal liquid. In both figures 3 and 4, the $S(Q)$ and $G(r)$ values for the higher temperature case have been displaced by 1 unit. The peak positions in $S(Q)$ and $G(r)$ and mean first shell coordination values are listed in table 1.

The peak positions in $S(Q)$ scaled by the nearest-neighbour distance, r_1, may be used to identify their character along the lines proposed by Price *et al* [38]. The first peak at, $Q_1 = 2.05$ Å^{-1} is typical of the first sharp diffraction peak found in network glasses. Assuming a density decrease of 20% for Al_2O_3 upon melting, the mean interatomic spacing d_s can be calculated to be 3.08 Å. From the $G(r)$ plot, the first peak at 1.76 Å may be taken to be the nearest-neighbour distance for the Al–O bond, r_1. The products $Q_1r_1 = 3.61$ and $Q_1d_s = 6.31$ shows that the first peak corresponds to intermediate-range order [38]. The second peak, $Q_2 = 4.5$ Å^{-1} gives $Q_2r_1 = 7.9$ and $Q_2d_s = 13.9$ which is indicative of topological short-range order, i.e., describing the touching Al–O pairs. If we consider the corundum structure of α-Al_2O_3, the prominent peak is from the {012} planes which has a $Q = Q_1 = 2\pi/d\{012\} = 1.80$ Å^{-1}. Further, if we average (weighted by intensity) all of the other major peaks in the 2.46–4.57 Å^{-1} range, we obtain an equivalent $Q_2 = 3.04$ Å^{-1}. For the liquid, $Q_1 = 2.05$ Å^{-1} and $Q_2 = 4.5$ Å^{-1}. The effect of melting is therefore to increase both Q_1 and Q_2. A peak which might be expected at a Q value between these two, due to chemical short-range order, is not observed, presumably because of the lack of contrast for x-ray scattering between Al^{3+} and O^{2-}.

The first peak at 1.76 Å is an unambiguous feature in $G(r)$. The ionic bond length is 1.72 Å based on the 0.36 and 1.36 Å ionic radii of Al^{3+} and O^{2-} atoms respectively [39] for tetrahedral coordination. Octahedrally coordinated aluminium (α-Al_2O_3) has a Al–O nearest-neighbour distance of 1.91 Å. This difference of 0.15 Å between the octahedrally and tetrahedrally coordinated aluminium is equal to the observed difference in bond length between

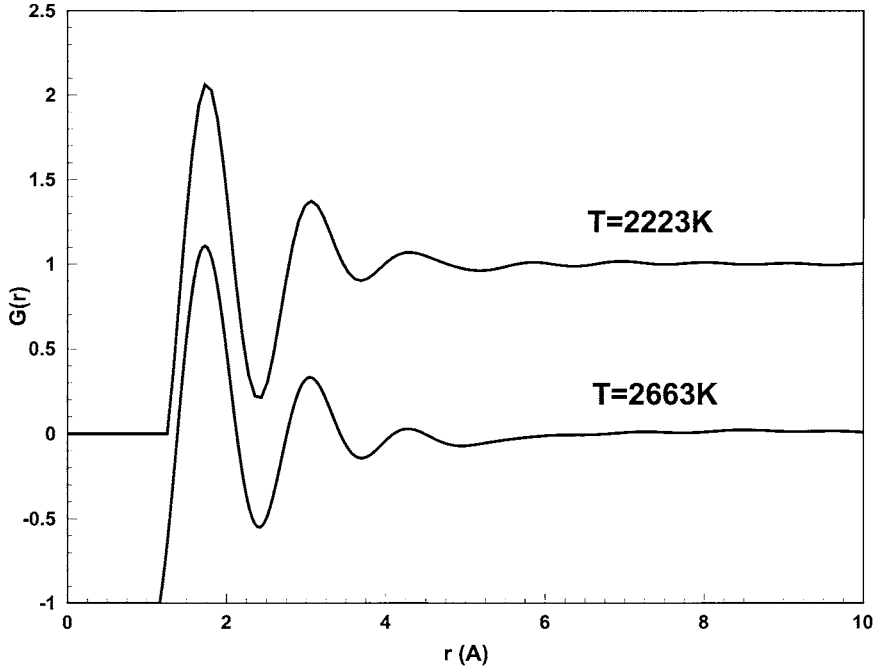

Figure 4. The pair distribution function, $G(r)$ for liquid Al_2O_3 at 2223 K (upper curve) and at 2663 K (lower curve). The $G(r)$ values for the lower curve have been shifted down by 1 for clarity.

octahedrally and tetrahedrally coordinated SiO_2 glasses [40]. If Al is tetrahedrally coordinated, then the shortest O–O distance is equal to $r_{Al-O} \times 1.633 = 2.87$ Å, while the shortest Al–Al distance will be $2r_{Al-O}\sin(\theta/2)$, where θ is the bond angle. If the second peak at 3.08 Å is a combination of O–O and Al–Al correlations, the bond angle must be larger than 122°. Integration under the first peak in $G(r)$ gives an Al–O coordination number of 4.4 ± 1, compared with the value of four expected from tetrahedral coordination. A large fraction of these AlO_4^{5-} may then link with other tetrahedral units by a combination of edge and corner sharing similar to that which occurs in γ-Al_2O_3. This type of arrangement can explain the small peak in $g(r)$ at 4.25 Å which would arise from Al–O interactions if tetrahedral AlO_4^{5-} units share an apex atom. We note that the assignment of the second and third peaks in $G(r)$ in our original article [13] was incorrect, as deduced by two separate molecular simulations (see below).

The observation of an Al–O nearest-neighbour distance of 1.76 Å clearly demonstrates that the coordination number for Al is reduced from six in the solid state to approximately four in the liquid. The observation of tetrahedrally coordinated aluminium is in excellent agreement with previous ^{27}Al MAS NMR measurements on liquid Al_2O_3 which give a mean coordination of 4.5 ± 1 for the liquid [37, 38, 41]. Four-coordinated aluminium is also observed in rapidly quenched alumina containing glasses and in binary oxide mixtures that are alumina rich. The present work on pure liquid Al_2O_3 provides direct confirmation of the NMR result.

The literature contains extensive information on the solidification behaviour of liquid alumina. When the cooling rates approach 10^5 K s^{-1}, amorphous alumina can be formed [42]. At somewhat lower cooling rates, the metastable γ-phase can be formed directly from the melt [42]. At cooling rates in the range of 1–100 K s^{-1}, only α-Al_2O_3 forms [43]. The present structural measurements are consistent with these observations. The enthalpy difference between γ- and α-forms is only 10 kJ mol^{-1} [44], which can be readily overcome

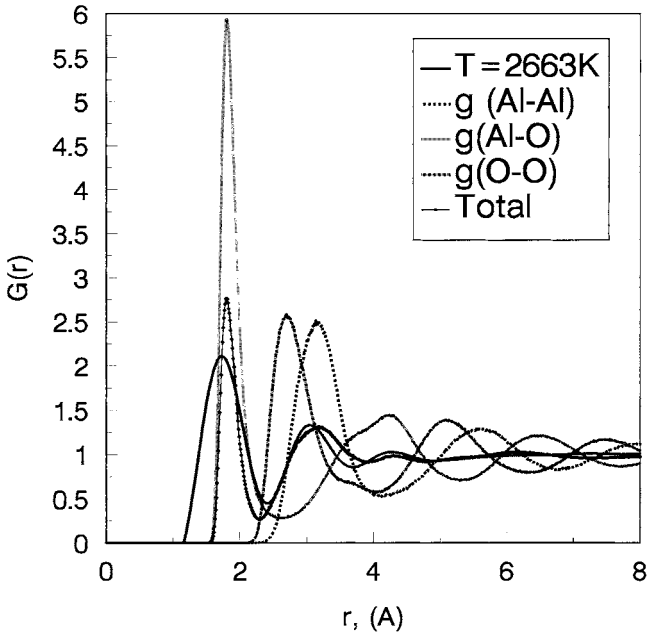

Figure 5. Comparison of the experimental $G(r)$ for liquid Al_2O_3 at 2663 K with the partial and total $g(r)$ correlations obtained from the molecular dynamic simulations of San Miguel *et al* [45] at $T = 2300$ K. The dark line is the experimental data, while the partial and total $g(r)$ curves are identified on the legend.

during solidification from the melt at the solidification temperatures. Liquid Al_2O_3 exhibits γ-Al_2O_3-like coordination, which leads to the possibility of the formation of an intermediate γ-phase prior to the formation of the stable α-phase during rapid solidification (e.g., recalescence).

These results on alumina stimulated molecular dynamics (MD) simulations by San Miguel *et al* [45] and by Hemmati *et al* [46]. The former used a modified Pauling potential, and were able to determine the temperature dependence of $S(Q)$ and $G(r)$ in the 2300–3000 K temperature range. Their x-ray weighted partial and total $G(r)$ values at 2300 K are given in figure 5 together with our $G(r)$ at 2663 K. It is evident that the second peak in the data is an average of the Al–Al and O–O correlations, while the third peak results primarily from Al–O second neighbour correlations, incompletely compensated by Al–Al and O–O correlations. San Miguel *et al* also found that tetrahedral Al was the predominant species (>50%) at all temperatures and that the fraction of octahedral alumina was exceedingly small. Hemmati *et al* [46] used a combination of a Born–Meyer potential together with a dipole polarization term to simulate the liquid. Their partial and total $G(r)$ values at $T = 2663$ K are plotted in figure 6 together with our experimental curve at $T = 2663$ K. While their partial $G(r)$ are essentially similar to those reported by San Miguel *et al* [45], they report a range of coordination numbers from four to six with abundances of 27.1%, 52.7% and 20.2% for four-, five- and six-coordinated Al^{3+}, respectively. Based on their observation of relatively slow exchange between four- and six-coordinated Al^{3+}, Hemmati *et al* suggested the possibility of phase separation between tetrahedral and octahedral alumina within the liquid, although there is no evidence of phase separation in rapidly solidified amorphous alumina [42]. The two MD simulations therefore disagree on the relative concentrations of tetrahedral and octahedral Al^{3+} ions, while producing an equivalent description for the equilibrium structure of the liquid.

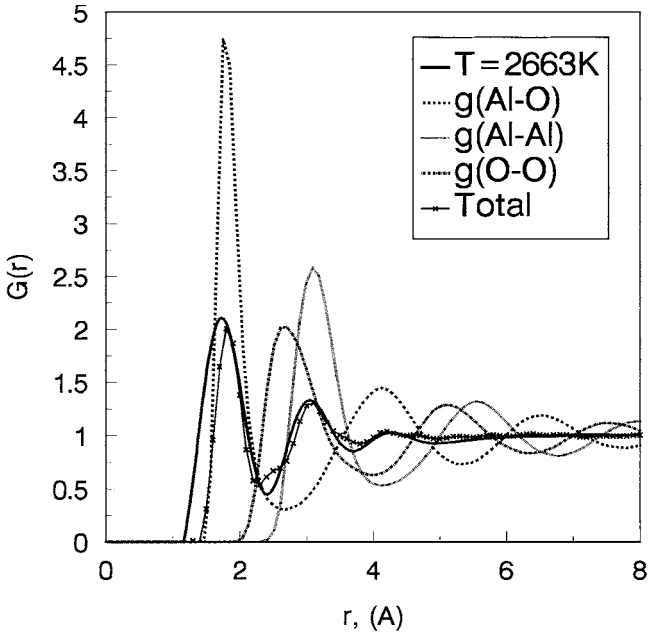

Figure 6. Comparison of the experimental $G(r)$ for liquid Al_2O_3 at 2663 K with the partial and total $g(r)$ correlations obtained from the molecular dynamic simulations of Hemmati *et al* [46] at $T = 2663$ K. The dark line is the experimental data, while the partial and total $g(r)$ curves are identified on the legend.

Lamparter and Kniep [47] have recently reported x-ray and neutron results on amorphous alumina. Both their x-ray-weighted and neutron-weighted $g(r)$ have peaks at 1.80 and 3.20 Å. These were ascribed to (Al–O), and the sum of (O–O) and (Al–Al) correlations, respectively, consistent with a tetrahedral structure with a bond angle between the tetrahedral units of 125° and an Al–O coordination of 4.1, rather similar to the present results for the liquid.

The presence of AlO_4^{5-} tetrahedral units in liquid Al_2O_3 would lead to moderate ionic conductivity. This has been confirmed in recent measurements by Enderby *et al* [48], who report an electrical conductivity of 6 ± 1 $(\Omega\ \mathrm{cm})^{-1}$ in the liquid just above the melting point.

3.1.2. Liquid yttrium oxide. Yttrium oxide (Y_2O_3) is extremely refractory with a melting point of 2731 K [49], 404 K higher than aluminium oxide. There is little information on the liquid state, but the thermodynamically stable form of Y_2O_3 forms the c-type rare-earth oxide structure [50], which is a defect CaF_2 structure in which the Y^{3+} ions occupy the centre of a distorted cube and the O^{2-} ions occupy six of the eight cube corners. Yttrium is more ionic than aluminium with a coordinate of 0.66 on Pettifor's scale compared with 1.66 for aluminium [51].

The x-ray weighted average structure factor $S(Q)$ for liquid Y_2O_3 is given in figure 7 at four specimen temperatures in the range 2526–3039 K [15, 16], two in the normal liquid and two in the supercooled liquid state. It can be seen that decreasing the temperature has the general effect of moving the first and second peaks in $S(Q)$ to *lower* Q values. Values of Q_2 were obtained by measuring the centroid of the peak rather than estimating the peak centre due to the shape and width of the peak. Values for the peak positions for the first two major peaks in $S(Q)$ at the four temperatures are given in table 1.

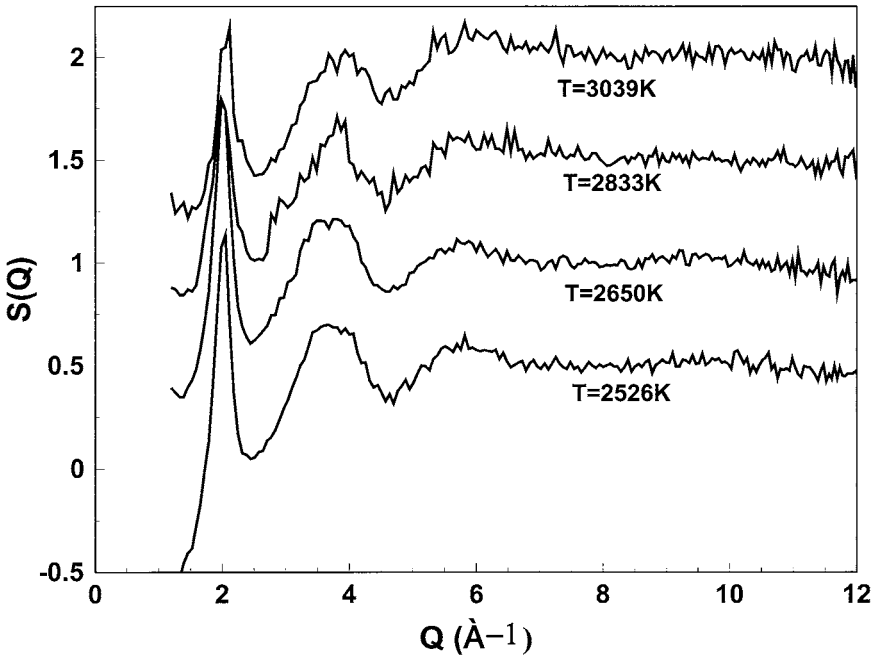

Figure 7. Structure factor for liquid Y_2O_3 at specimen temperatures of 3039, 2833, 2650 and 2526 K. The $S(Q)$ curves are displaced by 0.5 units for clarity.

Table 1. Structural results for liquid aluminium and yttrium oxides.

Temp. (K)	Q_1 (Å^{-1})	Q_2 (Å^{-1})	r_1 (Å)	r_2 (Å)	C_n (Y, O)
Liquid aluminium oxide, m.p. 2327 K					
2663	2.02	4.46	1.75 ± 0.03	3.06 ± 0.08	4.4 ± 1
2223	2.00	4.48	1.75 ± 0.03	3.05 ± 0.08	4.4 ± 1
Liquid yttrium oxide, m.p. 2731 K					
3039	2.12	3.93	2.23 ± 0.03	3.65 ± 0.08	7.5 ± 0.5
2833	1.98	3.81	2.24 ± 0.03	3.68 ± 0.08	7.7 ± 0.5
2650	1.98	3.74	2.25 ± 0.03	3.70 ± 0.08	6.4 ± 0.5
2526	2.05	3.68	2.27 ± 0.03	3.70 ± 0.08	6.3 ± 0.5

The positions of the peaks in $S(Q)$ can again be used to classify the ordering in the liquid. The first peak in $G(r)$ (see figure 8) may be taken as the nearest-neighbour distance r_1, and a number density of 0.060 Å^{-3} implies a mean interparticle spacing $d_s = 3.17$ Å. Taking average values of Q_1 and $Q_2 = 2.03$ and 3.79 Å^{-1}, respectively and a mean r_1 value equal to 2.25 Å (see figure 8 and table 1), the first and second peaks in $S(Q)$ correspond to $(Qr_1, Qd_s) = (4.57, 6.44)$ and (8.53, 12.01), respectively. The first two peaks in $S(Q)$ therefore represent chemical and topological short-range ordering. A peak below the low-Q limit of the data due to intermediate-range order cannot be ruled out, although any such peak is probably small since there is no upward turn in $S(Q)$ near the low-Q limit of the present data.

The significant trends in $S(Q)$ with decreasing temperature are the sharpening of the first and second peaks, a small shift to lower Q of the first peak and a 6% shift to lower Q of the second peak. The approximately 50% increase in the strength of the first peak in $S(Q)$ over the entire temperature range indicates increased definition of the first and second coordination shells as the liquid is supercooled.

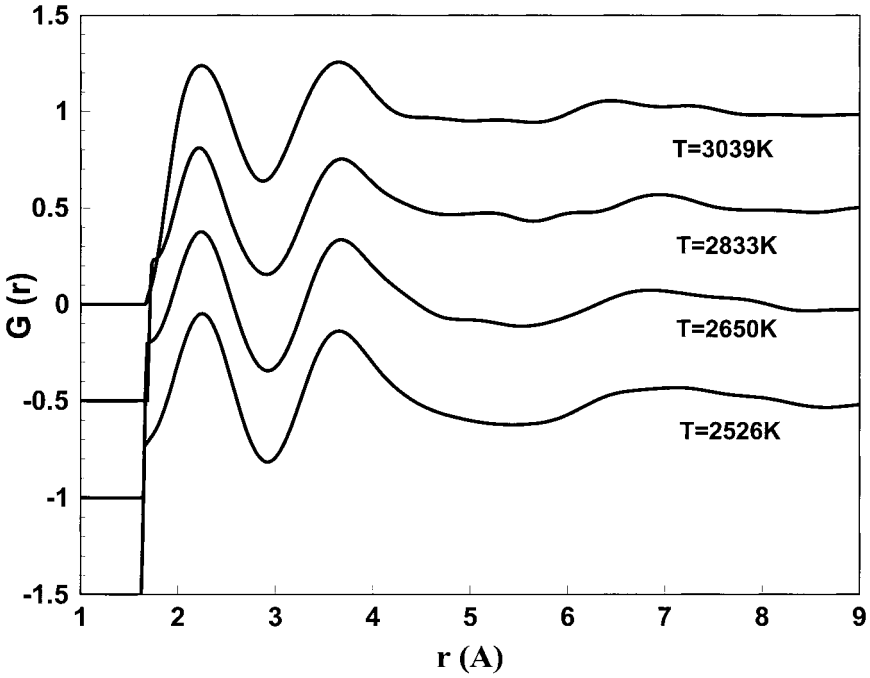

Figure 8. Pair distribution function for liquid Y_2O_3 at four specimen temperatures of 3039, 2833, 2650 and 2526 K. The $G(r)$ curves are displaced by 0.5 units for clarity.

The corresponding average x-ray weighted pair correlation function, $G(r)$, is shown in figure 8 for the same four temperatures. The two major peaks occur at about 2.25 and 3.65 Å, and additional features are observed at distances up to 8 Å. There is some temperature dependence of the positions of the first two peaks in $G(r)$. Values of the peak positions and their relative uncertainties are given in table 1. The values of the uncertainties are derived by applying uncertainties to the $S(Q)$ data before the Fourier transform. The first peak in $G(r)$ is at 2.23 Å at the highest temperature and at 2.27 Å at the lowest temperature. There is little or no change in the location of the second peak. The ionic radii for Y^{3+} and O^{2-} ions are 0.89 and 1.38 Å respectively [39], for Y and O atoms in sixfold coordination. For solid yttria in the *c*-type rare earth structure, the shortest and longest Y–O nearest-neighbours distances have been measured to be 2.26 and 2.35 Å, respectively [50]. The first peak in the liquid $G(r)$ therefore arises from Y–O nearest-neighbour pairs. The mean coordination values and their relative uncertainties, determined by integration under the first peak in $G(r)$, are also given in table 1. The mean coordination decreases with decreasing temperature from 7.5 ± 0.8 at high temperature to 6.3 ± 0.8 at low temperatures. The decreased coordination at lower temperatures is accompanied by a *longer* Y–O interionic distance. The *increase* in bond lengths and *decrease* in coordination number and Q values as the liquid is cooled are unusual. It appears that, at high temperature, the short-range structure of the liquid resembles the fluorite structure ($C_n = 8$), while in the supercooled state the short-range structure in the liquid tends towards the c-type rare-earth structure ($C_n = 6$). In addition, as the temperature is decreased, there is increased distinction between the first and second coordination shells, i.e., a deeper minimum in $G(r)$ between the first and second shells. This behaviour is characteristic of strongly ionic liquids [52].

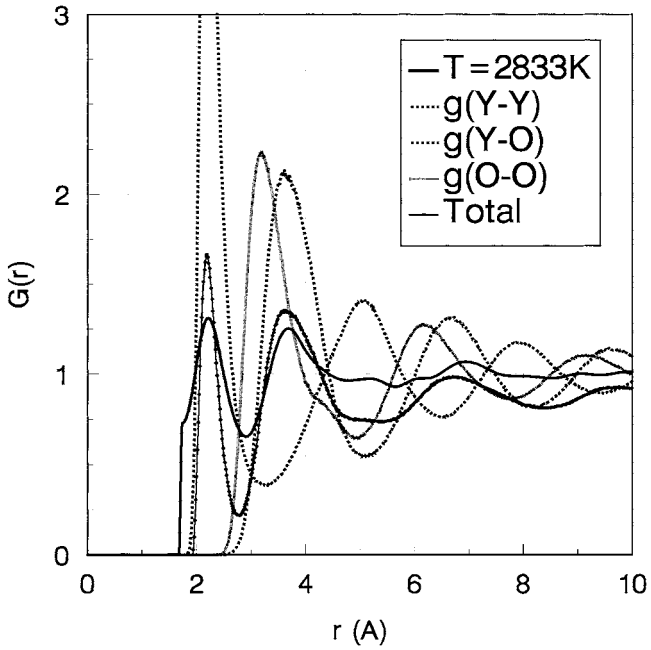

Figure 9. Comparison of the experimental $G(r)$ for liquid Y_2O_3 at 2833 K with the partial and total $g(r)$ correlations obtained from the molecular dynamic simulations of Alvarez *et al* [53] for $T = 2850$ K. The dark line is the experimental data, while the partial and total $g(r)$ curves are identified on the legend.

Alvarez *et al* [53] performed an MD study using a modified Pauling-type potential and derived the major structural features of the liquid. Their results indicate that the temperature dependence of the structural properties can be explained by allowing for oxygen loss in the system, i.e., changes in stoichiometry. The Y^{3+} coordination is about six and constant with temperature, and the O–O and Y–O correlations overlap on the high-r side of the first peak in $G(r)$. They suggest that this overlap results in an overestimation of the Y coordination since the area under the first peak includes contributions from the O–O correlations. Second, they show that the best fit to the measured $S(Q)$ and $G(r)$ is obtained for a stoichiometry of $Y_2O_{2.75}$, implying a loss of oxygen during heating to high temperatures. The temperature dependence of the Y–O bond distance was attributed to a change in oxygen vacancy concentration with temperature. Figure 9 shows a plot of the total and partial x-ray weighted $G(r)$ functions obtained from the MD simulations of Alvarez *et al* [53] at $T = 2850$ K together with our experimental data at 2833 K. It is evident that the MD simulations reproduce the experimental data well. The primary peak is the Y–O correlation, while the second peak is predominantly from Y–Y correlations, although O–O correlations contribute significantly to both peaks. The key question is whether such a large change in stoichiometry could occur in the liquid under the oxidizing conditions employed in the experimental study. It is to be noted that a 1.8% total mass loss was reported in our experiments which were conducted in air. Based on available thermochemical data for yttrium oxide, the mass loss would lead to a nearly equal loss of Y and O atoms, which would not change the stoichiometry to the extent that is suggested by the simulations.

Considering that solid Y_2O_3 is substantially more ionic than solid Al_2O_3, and that the ionic character may be expected to become more pronounced with increasing temperature,

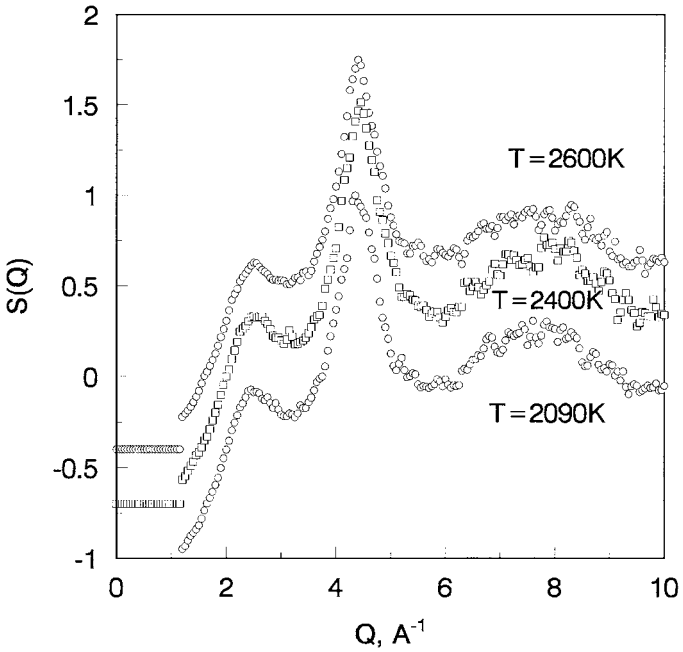

Figure 10. The x-ray structure factor for liquid boron at three temperatures of 2600, 2400 and 2090 K, The upper curves are displaced by 0.5 and 1 unit for clarity.

liquid Y_2O_3 may be predicted to have an electrical conductivity at least an order of magnitude larger than that of liquid Al_2O_3. It is also interesting to note a parallel behaviour with the chlorides, where YCl_3 preserves octahedral coordination on melting while $AlCl_3$ undergoes a structural rearrangement on melting into a tetrahedrally coordinated structure based on Al_2Cl_6, the species observed in the vapour [54].

3.2. The structures of liquid boron and silicon

3.2.1. Liquid boron. The crystalline forms of boron embody some of the most complex crystal structures for a pure element [55, 56]. Over 50 types of boron structure have been proposed in the literature, but it is now widely accepted that only three crystalline forms of boron, the α-rhombohedral, β-rhombohedral and tetragonal crystalline forms occur, the remaining structures resulting from stabilization due to impurity atoms. All of these crystalline forms are dominated by the B_{12} regular icosahedron structural unit. Amorphous boron has been investigated by Delplane *et al* [57] who reported that the short-range structure of the amorphous phase resembles the β-rhombohedral structure. The β-rhombohedral structure is the thermodynamically stable form at all temperatures below the melting point: the α-rhombohedral phase transforms to it above about 1200 °C [55]. In the α-rhombohedral phase each icosahedron is connected to other icosahedra by a combination of two- and three-centre bonds, so that the average coordination for boron atoms in this structure is 6.5 [55, 56]. In the β-rhombohedral structure, the icosahedra are surrounded by pentagonal pyramids giving rise to a 105-atom unit cell with an average coordination number of 6.6 [55]. The melting point of boron is 2360 ± 10 K.

Vast *et al* [58] performed *ab initio* molecular dynamics (MD) simulations of solid and liquid boron. They employed the local density approximation (LDA), a 48-atom cell and two different pseudopotentials to evaluate the structural properties and dynamics of the liquid.

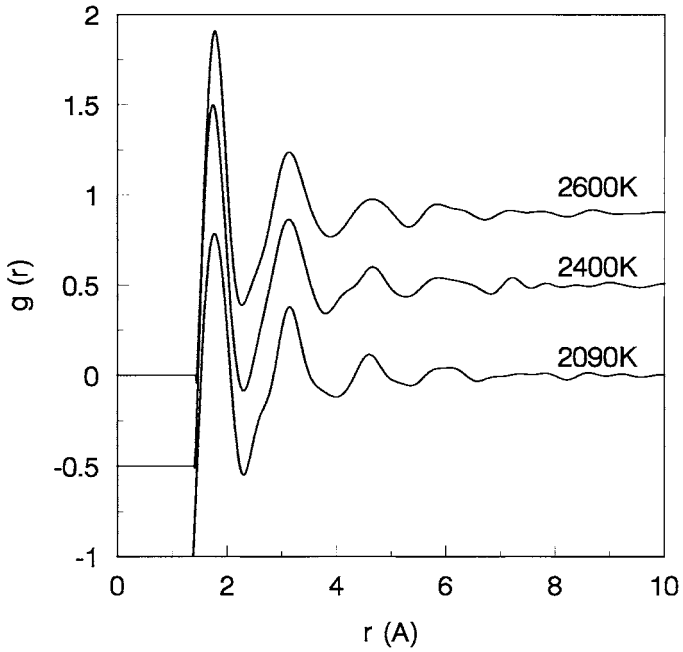

Figure 11. The pair distribution function for liquid boron at three temperatures of 2600, 2400 and 2090 K. The upper curves are displaced by 0.3 and 0.6 units for clarity.

Their results for the liquid at 2600 K gave peaks in $g(r)$ at 1.71 and 3.18 Å with an average coordination of about six. The structure exhibited broadened bond-angle distribution with peaks at 56 and 108° corresponding to the intraicosahedral bond angles; the corresponding peaks for the crystal occur at 60 and 108°. Bond angles corresponding to the intericosahedral bonds were noticeably absent. They concluded that icosahedral and pentagonal pyramidal arrangements of boron atoms are destroyed upon melting and that liquid boron assumes an open-packed structure with sixfold coordination.

The electrical conductivity calculated from the MD simulation is very high, about $2.5\times10^4\ \Omega^{-1}\ \mathrm{cm}^{-1}$ compared with $10^{-12}\ \Omega^{-1}\ \mathrm{cm}^{-1}$ in the solid at room temperature, consistent with an insulator–metal transition on melting. The electrical conductivity of liquid boron has not been measured. It can be estimated to be above $10^3\ \Omega^{-1}\ \mathrm{cm}^{-1}$ near the melting point from the fact that a 15 mm diameter can be rf heated at 450 kHz during zone refining operations.

The structure factor, $S(Q)$, for liquid boron measured at three temperatures of 2600 and 2400 K (normal liquid) and 2090 K (supercooled liquid), obtained at an x-ray energy of 14.9 keV is given in figure 10 [14]. At all three temperatures, $S(Q)$ is characterized by a weak first peak at approximately 2.5 $\mathrm{Å}^{-1}$ followed by the main peak located at 4.5 $\mathrm{Å}^{-1}$; on supercooling, there is a noticeable shift in the position of this peak to lower Q.

Figure 11 shows the pair correlation function, $g(r)$, for the same temperatures. The positions of the first two peaks in $g(r)$ (see table 2) are not affected by the large temperature change, but the r-values corresponding to the third and fourth peaks may be decreasing as the temperature decreases (see figure 11). The coordination number of boron atoms within the first coordination shell rises from about 5.8 ± 1.0 to 6.2 ± 1.0 as the liquid is supercooled.

Figure 12 compares the present $g(r)$ at 2600 K with that obtained by Vast *et al* [58] using *ab initio* molecular dynamics. The agreement is reasonable for the first and second peaks in $g(r)$ although the strength of the first peak in $g(r)$ is slightly greater for the MD data compared with

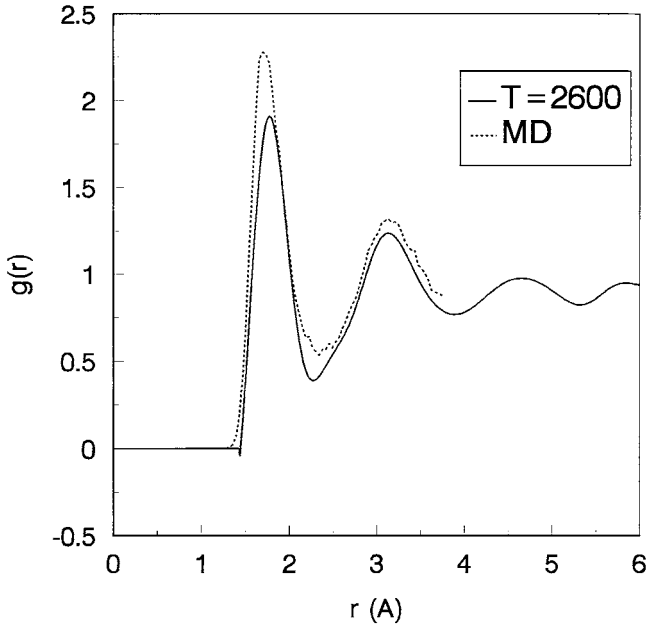

Figure 12. Comparison of the pair distribution function for liquid boron at 2600 K with the MD results obtained by Vast *et al* [58] for $T = 2600$ K.

Table 2. Comparison of short-range structural data for liquid, solid, and amorphous boron.

Phase	Temp. (K)	r_1 (Å)	r_2 (Å)	r_3 (Å)	C_n	Ref.
Liquid	2600	1.76 ± 0.03	3.15 ± 0.08	4.7 ± 0.1	5.8 ± 1	[14]
Liquid	2400	1.78 ± 0.03	3.16 ± 0.08	4.7 ± 0.1	5.8 ± 1	[14]
Supercooled liquid	2090	1.78 ± 0.03	3.15 ± 0.08	4.6 ± 0.1	6.2 ± 1	[14]
β	RT	1.803	3.03		6.6	[55]
α	RT	1.802	2.99, 3.58[a]	4.31	6.5	[55]
Amorphous	RT	1.80[b]	2.93[b]		6.4	[57]
MD	2600	1.71	3.18		6.0	[58]

[a] Double peak.
[b] Values obtained from the $g(r)$ plot differ slightly from those quoted in [55].

the experimental results. The MD calculations simulated only 48 atoms; hence there are no MD data at distances greater than about 3.5 Å. The MD simulations do not support a comparison with the experimental $S(Q)$ data because they did not extend to sufficiently small Q.

The pair correlation function at 2600 K is compared with those calculated for the α-rhombohedral, β-rhombohedral and tetragonal crystalline forms and for amorphous boron obtained by Delplane *et al* [57] in table 2 and figure 13. In order to compare these different phases, the first peak in $g(r)$ for the crystalline modifications of boron have been thermally broadened to correspond to room temperature. The three crystalline and amorphous boron phases are quite similar to the liquid in the region of the first peak, but differ in the location of the second and additional peaks. The results show that boron is unique among covalently bonded solids in undergoing an insulator–metal transition on melting but with a modest volume expansion and little change in the short-range structure.

In [57], the similarity between the β-rhombohedral and amorphous forms is cited as evidence for survival of the icosahedral units in the amorphous solid. The first sharp diffraction

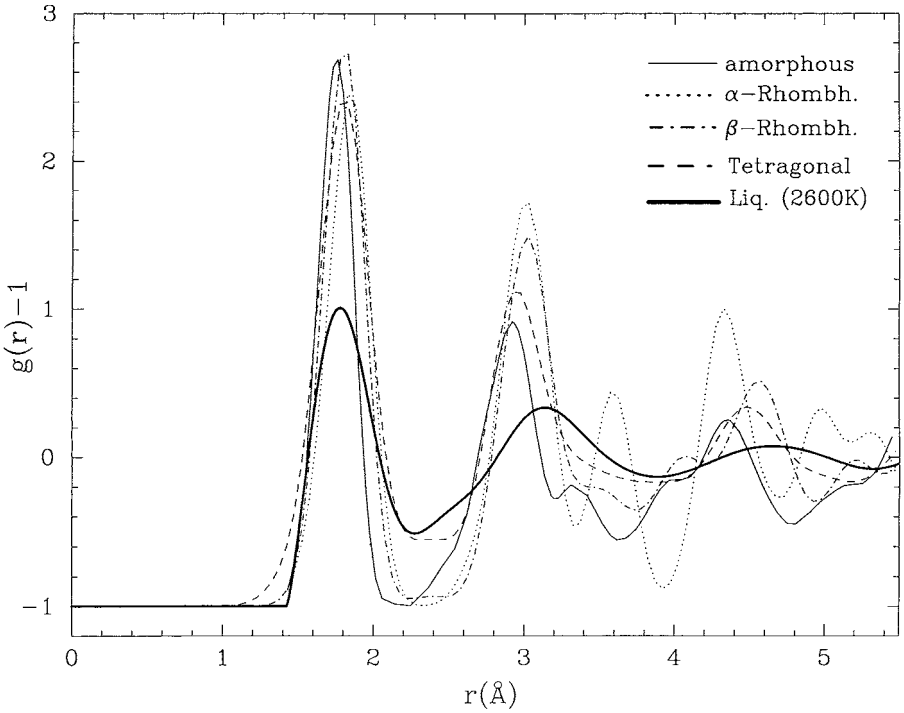

Figure 13. Comparison of the pair distribution function for liquid boron at 2600 K with those for the amorphous, α- and β-rhombohedral and tetragonal forms. $g(r)$ of the crystalline forms has been thermally broadened to correspond to room temperature.

peak observed in $S(Q)$ of the amorphous solid at low Q was ascribed to the presence of icosahedral clusters, since the random packing of units of diameter d is known to produce a peak at $Q \sim 2\pi/d$. However, an *ab initio* MD simulation of amorphous boron [59] did not produce such units, and it is known that network structures with an appropriate length scale can also produce such peaks [60]. The idea that B_{12} units survive in the amorphous solid [57] raises the question of whether they may survive in the liquid. The rather good agreement of the present results with the *ab initio* MD simulations of the liquid, which certainly do not contain these units might be taken as evidence against the survival of B_{12} units in the liquid. However, the restricted cell size of the MD calculation would make it difficult to incorporate such large units in the simulation. Evidence that suggests that B_{12} units may occur in the liquid, particularly as the liquid is supercooled, comes from (i) remarkable stability of these units when metallic atoms are added to the boron network, (ii) the observation of rather low surface tension [61], (iii) the limited range over which the liquid can be supercooled (only 11% of the melting temperature compared with most liquids which can be supercooled to about 20%) and (iv) slight differences in the structure of the supercooled liquid (shoulders on both sides of the second peak in $g(r)$).

Diffraction data obtained on the liquid down to 0.8 Å^{-1} did not yield a first sharp diffraction peak which, as discussed above, could be expected if significant numbers of icosahedra were present. In addition, the significant shifts and broadening of the second and third peaks suggest a different intermediate-range order in the liquid compared with the crystalline forms. In the α-rhombohedral form, the peaks in $g(r)$ at 2.99 and 3.58 Å correspond to icosahedral and inter-icosahedral bonding, respectively. The two shoulders that appear in $g(r)$ for the supercooled

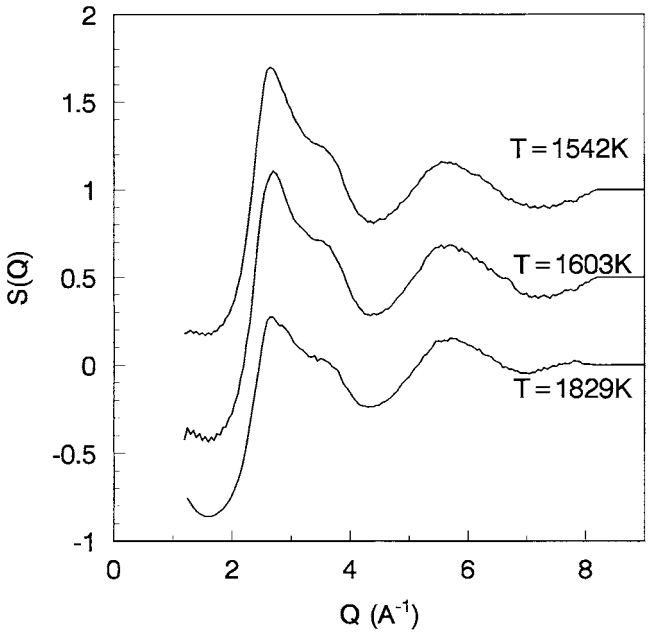

Figure 14. Total structure factor, $S(Q)$ for liquid Si at three specimen temperatures of 1542, 1603 and 1829 K. The melting point of Si is 1688 K. The $S(Q)$ curves have been shifted for clarity.

liquid are nearly at these distances, which might indicate the existence of a small number of B_{12} units. Overall, it is not possible to conclusively establish the presence or absence of icosahedra or pentagonal pyramids in the liquid.

3.2.2. Liquid Si. There has been recent interest in the liquid state properties of Si, Ge and other semiconductor materials. The literature contains conflicting and anomalous data on the density [62, 63], viscosity [64, 65], and electrical resistivity [66, 67] near the melting point. Because of the occurrence in Si (and Ge) of a semiconductor-metal transition upon melting accompanied by a 10% volume contraction, the structure of the supercooled liquid has been the subject of much speculation [68]. Both x-ray and neutron diffraction data and theoretical studies [69] on the liquid above the melting point show that Si and Ge are low-coordination metallic liquids with significant directional bonding. The main features of the diffraction patterns and electronic properties have been satisfactorily explained by *ab initio* MD studies [70–72]. However, the structural properties of the liquid in the supercooled state prior to the nucleation of the crystalline solid were not investigated prior to our recent paper on supercooled Si [12].

Figure 14 shows the average structure factors $S(Q)$ for liquid Si at temperatures of 1542, 1603 and 1829 K [12]. The melting point of Si is 1688 K, so that the two lower temperature measurements correspond to the supercooled liquid. $S(Q)$ shows a main peak with a pronounced shoulder on the high-Q side in addition to a second peak. Table 3 lists the locations of the peaks in $S(Q)$ for liquid Si, including values for the hump/shoulder. The most significant effect of supercooling is to move the first peak and shoulder to a Q value that is about 8% greater at 1542 K than at 1829 K. This is substantially larger than the linear thermal contraction (about 0.6%) over the same temperature range [63].

Pair correlation functions, $g(r)$, obtained from $S(Q)$ are given in figure 15. Supercooling results in a significant sharpening of the first peak and a reduction in the coordination number

Table 3. Summary of $S(Q)$ and $G(r)$ data for metallic liquids investigated in this study.

		$S(Q)$			$g(r)$				
Materials	Temp. (K)	Q_1 (Å^{-1}) ±0.03	hump (Å^{-1})	Q_2 (Å^{-1}) ±0.03	r_1 (Å) ±0.03	sub1 (Å)	sub2 (Å)	r_2 (Å) ±0.05	C_n (atoms) ±0.5
Present work									
Si	1829	2.45	3.55	5.45	2.46	3.45		5.20	6.4
Si	1603	2.70	3.60	5.70	2.42	3.27	3.95	5.22	5.6
Si	1542	2.65	3.65	5.65	2.41	3.28	3.98	5.22	5.6
Ni	2035	3.08		5.32	2.54			4.58	11.8
Ni	1732	3.08		5.28	2.53			4.70	11.9
Ni	1606	3.08		5.32	2.49			4.54	11.9
Ni	1548	3.08		5.40	2.49			4.58	11.9
Cu	1770	3.05		5.70	2.55			4.74	10.9
Al	1450	2.57		4.95	2.82			5.33	11.5
Literature data (experimental results)									
Si [73]	1800	2.63	3.55	5.68	2.46	3.64		5.64	6.2
Ni [79]	2023	3.02		5.80	2.40			4.50	11.6
Cu [79]	1723	3.0		5.5	2.50			4.70	11.3
Cu [84]	1833	3.0		5.5	2.5			4.7	
Al [85]	1323	2.7		5.0	2.8			5.1	11.5
Al [86]	953	2.7		4.95	2.79			5.21	

from 6.4 to 5.6. A systematic decrease of 2% in the position of the first peak is observed with supercooling, as given in table 3, again considerably larger than the linear contraction in the structure. The stable liquid shows a shoulder on the high-r side of the first peak, which splits into a double shoulder upon supercooling. The r-values corresponding to these features are also given in table 3.

The pair correlation function, $g(r)$, for the stable liquid ($T = 1829$) is compared with the experimental measurements of Waseda [73] at $T = 1793$ K in figure 16. The agreement is quite good for the major features in $g(r)$, but some differences near the shoulder region are evident. *Ab initio* MD simulations of liquid Si at 1800 have been performed by Stich *et al* in the LDA [70, 71] and in the generalized gradient approximation with inclusion of spin (SGGA) [72]. In figure 16 we include the results obtained from the SGGA, which show a narrower and sharper first shell. This may arise from the limited cell size of the MD and its inability to maintain the directional bonding into the second coordination shell.

Liquid Si is metallic [69, 74] with a coordination number of about six, indicating an open structure compared to other liquid metals. This indicates that some fraction of the directional bonds survive upon melting. The most significant effect of supercooling is to split the shoulder in $g(r)$ at 3.45 Å into two features at 3.28 and 3.95 Å. The appearance of the double shoulder suggests a tendency towards tetrahedral covalent bonding in the supercooled state. Extrapolation of the coordination numbers at the supercooling limit (about 340 K of supercooling) yields a value of 4.6. Thus, nearly all the atoms in the liquid may be covalently bonded at this limit.

The reduction in coordination with supercooling is an interesting result which has been previously suggested by several MD simulations that have employed the Stillinger–Weber potential to study the supercooled state [75, 76]. Angell and Borick [77] have pointed out that the reduction in coordination with supercooling observed in Si provides support for the idea of a liquid–liquid phase transition. Their MD simulations predict a reduction in coordination to 4.6 near the supercooling limit ($T = 1350$ K) followed by a transition to a four-coordinated

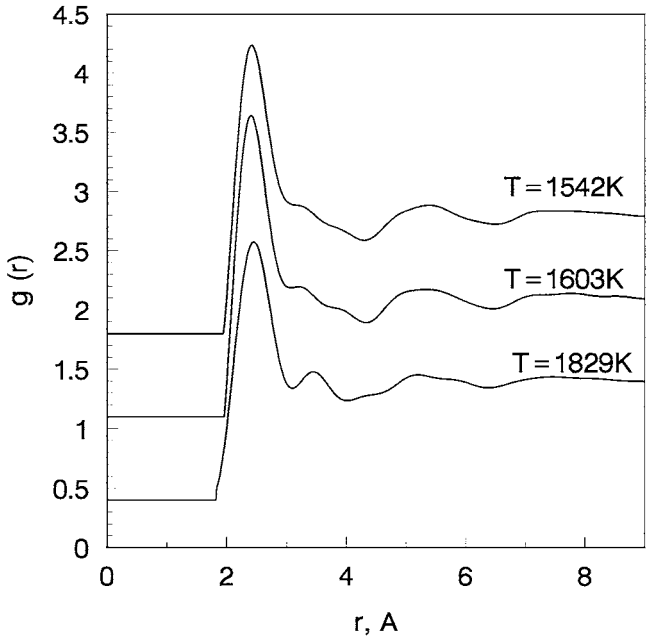

Figure 15. Pair distribution function, $g(r)$ for liquid Si at three specimen temperatures of 1542, 1603 and 1829 K. The melting point of Si is 1688 K. The $g(r)$ curves have been shifted for clarity.

amorphous semiconducting liquid. Angell and Borick argue, on the basis of diffusion data, that the four-coordinated semiconductor is liquid just below the transition. The reverse transition has been observed in laser melting studies of amorphous silicon [78]. It would be interesting to search for such a structural transition in Si, Ge and other III–V semiconductors by time-resolved x-ray measurements. We should point out the density of supercooled Si [63] extrapolates to a density maximum around 1200 K, considerably lower than the temperature at which the simulations predict a polymorphic liquid–liquid phase transition.

3.3. Structures of selected metallic liquids

3.3.1. Liquid nickel. X-ray diffraction measurements for liquid nickel were obtained over a wide range of temperature, 1548–2035 K, including the supercooled state. The melting point of nickel is 1726 K. Figure 17 shows the $S(Q)$ results for liquid nickel at temperatures of 1548, 1606, 1732 and 2035 K. However, these data were obtained over a relatively short Q-range of 0.8–7 Å^{-1}, which made the data analysis more difficult. We thus assign a larger uncertainty to the overall measurements, but the relative error between the different data sets is considerably smaller. Q-values for the peaks in $S(Q)$ are listed in table 3.

$S(Q)$ for liquid Ni is characterized by a strong first peak centred at 3.1 Å^{-1} and a second peak centred at about 5.3 Å^{-1}. The effect of temperature is twofold: first, there is a 10% narrowing of the primary peak as the high-temperature liquid is supercooled to 1548 K. Second, there is about a 17% enhancement of the first peak intensity, consistent with a more localized short-range structure. Using the number density of 0.079, and a mean interparticle spacing, d_s equal to 2.89 Å, and using mean values of Q_1 and Q_2 equal to 3.08 and 5.30 respectively, the reduced wave vector values $Q_1 r_1 = 7.73$ and $Q_1 d_s = 8.90$ classify the peak as arising from topological short-range order.

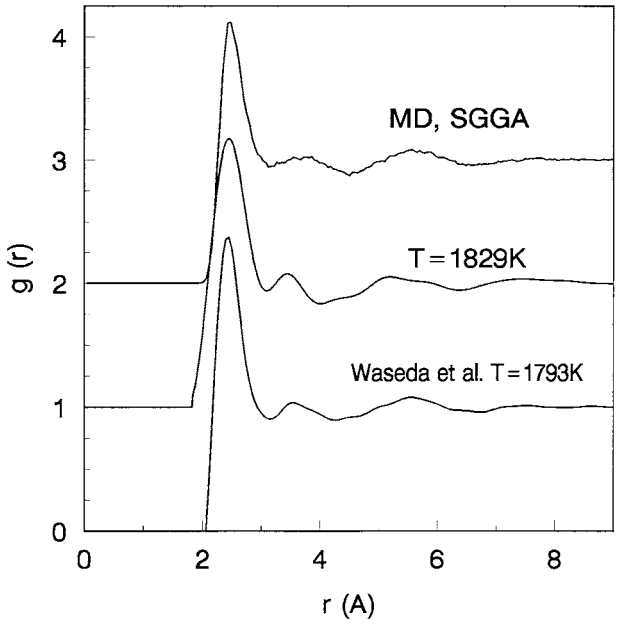

Figure 16. Comparison of the pair distribution function of liquid Si at $T = 1829$ K with the results from the *ab initio* MD simulation of Stich *et al* [72] and the x-ray results from Waseda *et al* [73]. The $g(r)$ curves have been shifted for clarity.

The pair correlation function, $g(r)$, for liquid Ni is given in figure 18 for the same four temperatures. $g(r)$ is characterized by a primary peak centred near 2.5 Å and a second peak at 4.6 Å; additional peaks are observed at distances up to 9 Å or greater. There is little or no effect of temperature on the position of the first peak in $g(r)$; values of the first two peaks in $g(r)$ are listed in table 3. The first-shell coordination values calculated from an integration of the first peak in $g(r)$ are unaffected by temperature over the entire temperature range. The first-shell coordination is nearly 12 for all temperatures (see table 3). The second peak in $g(r)$ undergoes some sharpening as the temperature is lowered.

The significant result for liquid Ni is that little or no change occurs in the short- and intermediate-range structure over the wide temperature range studied. The only visible effect of temperature appears to be a slight sharpening of the peaks in $g(r)$, but no significant change in the first-shell coordination (which remains around 12). The first-neighbour distance decreases from 2.54 to 2.49 upon cooling the liquid from 2035 to 1542 K. It appears from these results that the structure is literally frozen in as the liquid is cooled below its melting point. This implies that the liquid is unlikely to exhibit any large changes in heat capacity or other thermal or electronic properties as it is supercooled.

Figure 19 compares the present $g(r)$ results for liquid nickel at $T = 2035$ K with the previously published results of Waseda [79]. There is good agreement in the overall peak positions, but the present results for nickel exhibit a wider first and second coordination shell.

3.3.2. Liquid 80% Co–20% Pd. Liquid 80% Co–20% Pd has been a subject of much attention recently. Platzek *et al* [3] first reported that the liquid exhibited magnetic ordering when supercooled to temperatures below the Curie temperature of the solid phase. Subsequent studies investigated the specific heat capacity [80], magnetization and magnetic susceptibility [81],

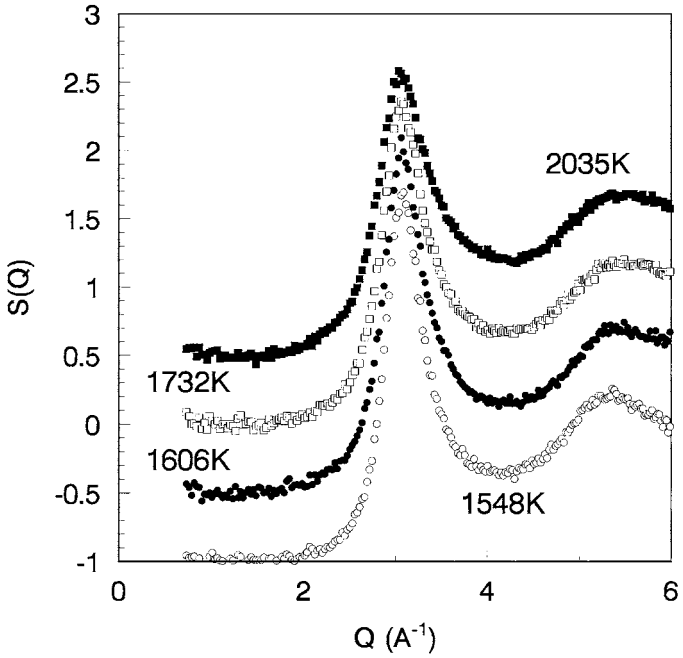

Figure 17. Structure factor, $S(Q)$ for liquid Ni at four specimen temperatures of 2035, 1732, 1606 and 1548 K. The melting point of nickel is 1726 K and the lower two curves correspond to supercooled liquid Ni. The $S(Q)$ curves have been shifted for clarity.

undercooling behaviour [82] and solidification behaviour [83] of this liquid. All of this prior work pointed to the occurrence of magnetic ordering when the liquid was undercooled to temperatures below the Curie point of the solid phase. The currently accepted solidus and liquidus temperatures for this alloy are 1561 and 1606 K, respectively; the Curie point of the solid phase occurs at 1271 K, while the liquid can be undercooled to temperatures as low as 1251 K.

Jacobs and Egry [25] undertook an EXAFS study of undercooled Co–Pd melts to investigate the possibility of structural changes that might accompany magnetic ordering in the liquid state. Their EXAFS measurements were obtained at the cobalt K edge ($E_0 = 7.709$ keV) over a wide temperature range and included the liquid undercooled by up to 300 K, below the Curie point temperature of the solid phase. From their EXAFS results, they were able to extract the nearest-neighbour distances and Debye–Waller factors, but were unable to find any major structural changes in the liquid accompanying magnetic ordering.

We have recently reported the results of x-ray scattering studies on liquid and supercooled liquid 80% Co–20% Pd. Figure 20 shows the average structure factor, $S(Q)$, for liquid 80% Co–20% Pd at three specimen temperatures of 1788, 1638 and 1480 K. The lowest temperature corresponds to liquid supercooled by 126 K. The temperature dependence of $S(Q)$ is only slight. The first peak in $S(Q)$ has a small shoulder on the low-Q side that appears to decrease in strength as the temperature is reduced.

The corresponding $G(r)$ curves at the same three temperatures are plotted in figure 21. In addition to the main peak at $r = 2.55$ Å, there is evidence for a shoulder on the high-r side of the first peak which is more pronounced at lower temperature.

The main peak positions in $S(Q)$ and $G(r)$ are listed in table 4. On supercooling, the mean first-nearest-neighbour distance is lowered from 2.57 to 2.54 while the second- and third-nearest neighbour distances increase.

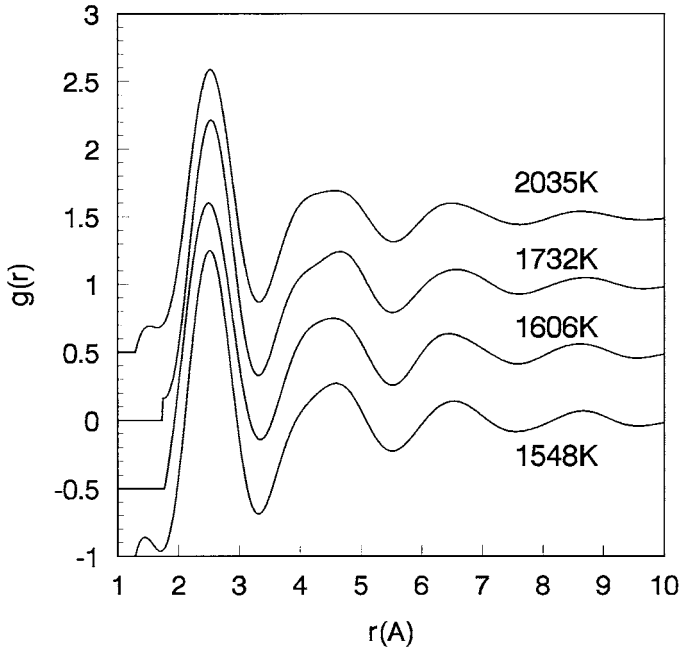

Figure 18. Pair distribution function, $g(r)$, for liquid Ni at four specimen temperatures of 2035, 1732, 1606 and 1548 K. The melting point of nickel is 1726 K and the lower two curves correspond to supercooled liquid Ni. The $g(r)$ curves have been shifted for clarity.

Table 4. Peak positions in $S(Q)$ and $G(r)$ for liquid 80% Co–20% Pd.

Temperature (K)	Q_1 (Å^{-1})	Q_2 (Å^{-1})	r_1 (Å) (±0.03)	r_2 (Å) (±0.08)	r_3 (Å) (±0.1)
1788	2.96	5.44	2.57	4.60	6.7
1638	2.92	5.48	2.58	4.68	6.7
1480	2.96	5.44	2.54	4.78	6.9

Coordination numbers were derived by integrating over the first peak in $N(r) = 4\pi\rho_a r^2 G(r)$. In view of the shoulder on the high-r side, areas were computed separately for the symmetric part (obtained by reflecting the part to the left of the peak centre about the centre) and the residual asymmetric part. Coordination numbers derived on the assumption of complete disorder (the Co and Pd atoms are placed randomly on each atomic position) are given in table 5. Again, no systematic temperature dependence is observed.

The results for the alloy can be compared with data in the literature on pure liquid Co and Pd [79]. In figure 22 we compare $G(r)$ for the alloy at $T = 1480$ K together with a weighted average of the $g(r)$-values for pure Co and Pd given by:

$$\langle G(r)\rangle = \frac{C_1 Z_1^2 g_1(r) + C_2 Z_2^2 g_2(r)}{C_1 Z_1^2 + C_2 Z_2^2} \tag{7}$$

where C_i is the molar concentration, Z_i is the atomic number and $g_i(r)$ the pair distribution function for element i. For the present case, $C_1 = 0.8$, $C_2 = 0.2$, $Z_1 = 27$ and $Z_2 = 46$ and the $g(r)$ for Co and Pd were taken from [79]. It can be seen that the weighted $G(r)$ produces a good match with the measured results, suggesting that the liquid structure can be approximated rather well by a random mixture of Co and Pd atoms.

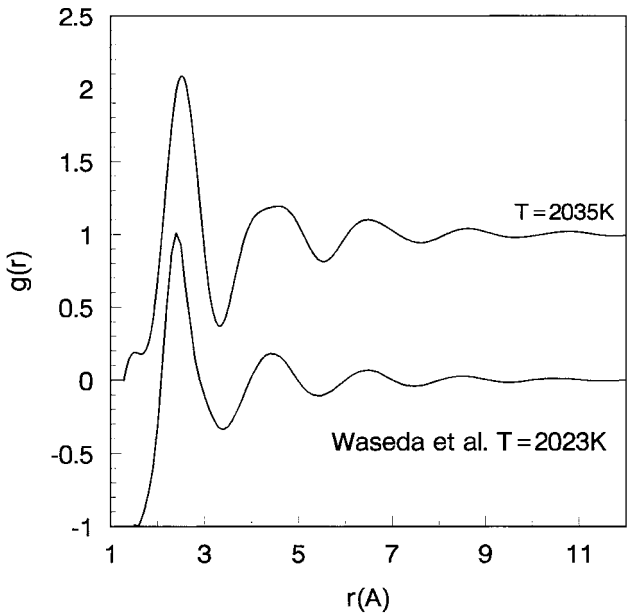

Figure 19. Comparison of the $g(r)$ for liquid Ni at 2035 K with the results of Waseda [79]. The $g(r)$ curves have been shifted for clarity.

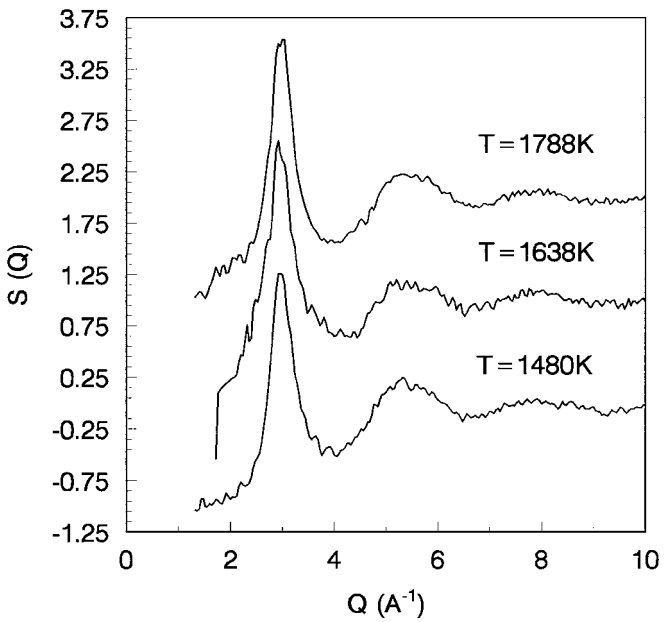

Figure 20. Total structure factor for liquid 80% Co–20% Pd at 1788, 1638, and 1480 K. The liquidus temperature for the alloy is 1606 K. The curves have been displaced by 1 unit for clarity.

The present results do not show a dramatic change in the structure of liquid 80% Co–20% Pd as the liquid is supercooled, consistent with the notion that the onset of the magnetic ordering corresponds to a first-order transition. Thus, in supercooling to temperatures above the transition, the liquid structure may be expected to change slowly.

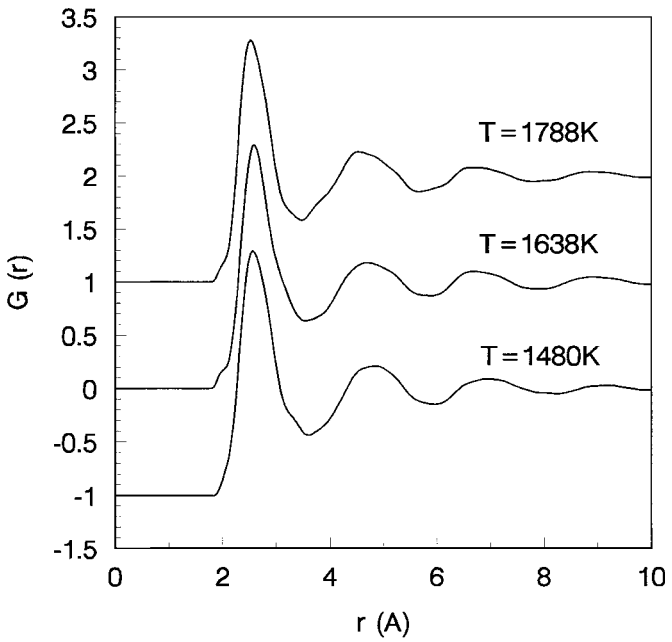

Figure 21. Pair distribution function for liquid 80% Co–20% Pd at 1788, 1638 and 1480 K computed using the maximum-entropy Fourier transform method. The liquidus temperature for the alloy is 1606 K. The curves have been displaced by 1 unit for clarity.

Table 5. First-nearest-neighbour coordination for liquid 80% Co–20% Pd.

	Coordination (±0.5)		
Temperature (K)	Primary	Residual	Total
1788	7.00	2.41	9.41
1638	8.04	2.92	10.96
1480	7.89	2.40	10.29

Jacobs and Egry [25] have conducted an EXAFS study of deeply supercooled 80% Co–20% Pd and have reported the mean Co–Co and Co–Pd distances as 2.51 and 2.56 Å respectively, and that these mean distances did not change significantly with temperature. Our result for the x-ray weighted nearest-neighbour distance agrees well with their value for the Co–Pd distance. It remains to be seen if there are any changes to the structure at temperatures below the Curie temperature of the solid phase.

3.3.3. Other metallic liquids. We include in table 3 results obtained on liquid Al and Cu at temperatures far in excess of their respective melting points; no structural data were obtained in the supercooled regime for these liquids. Table 3 also includes data from the literature for Al and Cu that shows good agreement of the present results with these previous measurements.

3.4. Ordering in liquids

It is useful to consider classification of the structural properties of these high-temperature liquids according the scheme proposed by Price *et al* [38]. In this scheme, the two main peaks in $S(Q)$ may be used to identify the type of ordering that may exist in the liquid or

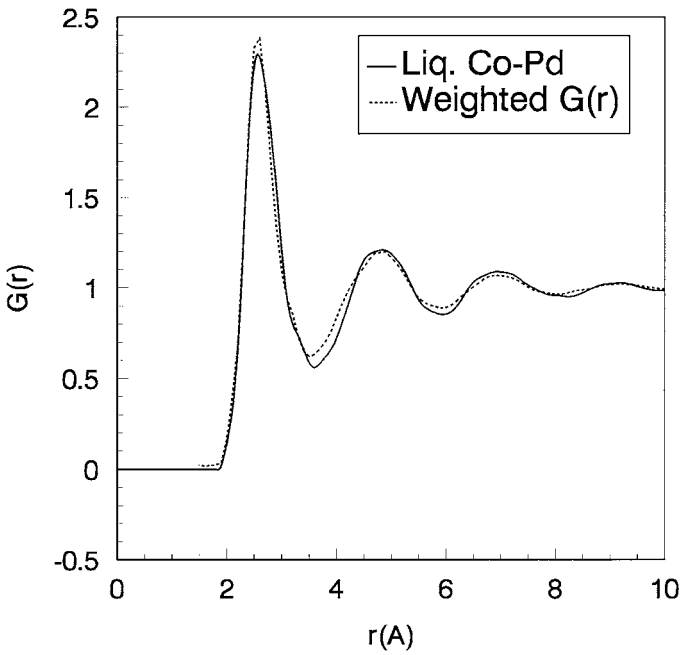

Figure 22. Pair distribution function for liquid 80% Co–20% Pd at 1480 K compared with the weighted average of the $g(r)$ values of pure Co and Pd (see equation (7)).

glass by scaling the Q_i appropriately with r_1, the first-nearest-neighbour distance, and d_s, the mean interparticle spacing. Values of Q_1, Q_2, and r_1 have already been tabulated in this article. Figure 23 gives the plot of $Q_i r_1$ against $Q_i d_s$ for all of the liquids studied by combined levitation and x-ray diffraction techniques. The solid line drawn in the figure represents the limit for dense random packing of hard spheres, and it can be readily seen that all of the metallic liquids fall close to this line. It can also be seen that the molten oxides, Si and B exhibit open structures.

4. Summary

In this paper we have:

(i) described the use of containerless techniques in conjunction with x-ray diffraction;
(ii) provided a detailed description and techniques employed in conical nozzle levitation (CNL) of molten materials including instrumentation used to monitor and control the specimen position, temperature and stability;
(iii) discussed methods used to analyse x-ray data and corrections applied to x-ray data for the case of scattering from spherical droplets;
(iv) presented the results of x-ray diffraction studies on liquid aluminium oxide in the normal and supercooled states. The key findings include the change in the aluminium coordination from octahedral to tetrahedral upon melting and the hypothesis that these AlO_4^{5-} tetrahedral units are connected through corner sharing. The liquid alumina results were compared with two recent MD studies [46, 47] that produce results in good agreement with the experimental findings. The two MD studies, however, disagree on the relative abundances of the four- and six-coordinated Al^{3+} ions;

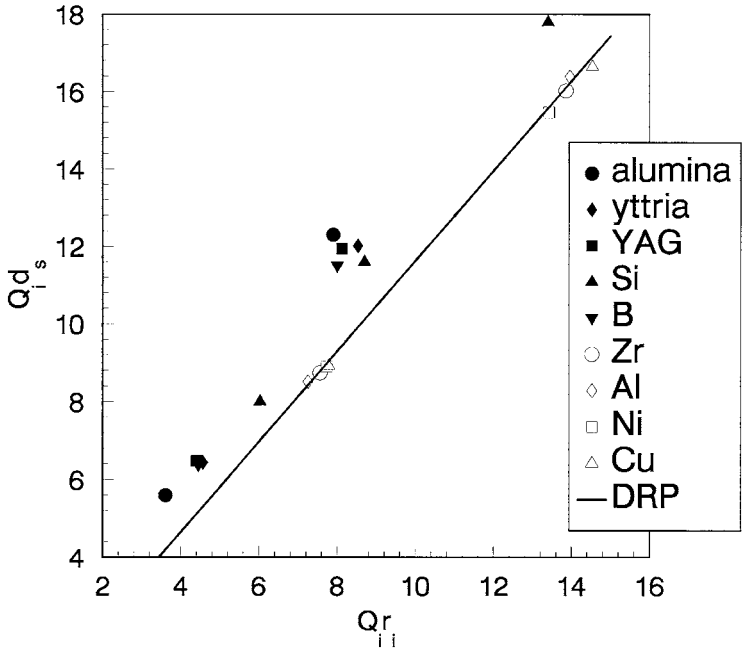

Figure 23. Plot of the values of $Q_i d_s$ against $Q_i r_1$ for all of the liquids studies by levitation and x-ray techniques. For liquid Si, the location of the shoulder in $S(Q)$ contributes an extra value on the plot. See text for further details.

(v) presented a summary of our findings on liquid yttrium oxide including the $S(Q)$- and $G(r)$-values for the normal and supercooled liquid states. Supercooling results in an apparent reduction in first-shell coordination and an increase in the Y–O bond length. A coordination number in excess of seven is observed at higher temperatures. The unusual changes in bond length and coordination have been explained by a recent MD study [54], and the results are compared in this paper;

(vi) presented results on the changes in the atomic structure with supercooling for liquid Si, which exhibits a significant reduction in first-shell coordination and a splitting of the shoulder on the high-r side of the first peak in $g(r)$. The data for the normal liquid are in good agreement with the previous experimental measurements of Waseda *et al* [73] and the *ab initio* MD simulations of Stich *et al* [70–72]. The changes in the coordination with supercooling are consistent with recent MD simulations [78] which predict a gradual reduction in first-shell coordination followed by a polymorphic liquid–liquid phase transition in Si near the bulk supercooling limit;

(vii) discussed recent experimental results on liquid boron. The results show that the short-range structure is surprisingly similar to that of the crystalline and amorphous forms of boron, with little change in bond length but a broadening of the first coordination shell, preserving the coordination around six. Agreement with the *ab initio* MD results [58] for the normal liquid is reasonably good, given the restricted cell size of the MD simulation. The existence of icosahedral clusters in the liquid is discussed but no conclusive statement can be made about their existence. Boron appears to be unique among solids that undergo an insulator to metal transition upon melting in that this is accompanied by a small volume expansion and little change in the short-range structure;

(viii) included the first results on the atomic structure of liquid Ni studied over a 500 K temperature range, including 200 K in the supercooled regime. The results show that the liquid structure appears to be 'frozen' with little change in $S(Q)$ over the temperature range investigated. Based on these results, little or no change in thermophysical and electronic properties is predicted for Ni as a function of supercooling;

(ix) presented recent measurements of the atomic structure of liquid 80% Co–20% Pd alloy. This alloy has been reported to exhibit magnetic ordering when the liquid is cooled below the Curie temperature of the solid phase. The present results, which did not achieve the necessary supercooling, show rather little temperature dependence of the structure. A simple model for the liquid structure indicates a random arrangement of Co and Pd atoms in the first and second coordination shells.

5. Future prospects

It is clear that the body of structural work employing levitation techniques just scratches the surface. One can foresee crucial extensions of the work reported in this article, including the following.

(i) Generalization of the studies of supercooled liquid silicon to supercooled melts of analogous III–V and II–VI semiconductors. Although many of these systems have been studied just above the melting point, investigations of the supercooled state may reveal new types of liquid–liquid phase transition in addition to identification of new metastable phases of these compounds.

(ii) The magnetic ordering identified by the Cologne group in Co–Pd alloys is possibly just one member of a large class of magnetically ordered liquid states waiting to be discovered. It is worthwhile to perform additional structural measurements on these types of liquid at temperatures closer to the Curie points of the corresponding solid phases.

(iii) Molten YAG remains the only liquid for which a phase transition between two liquids of the same composition is well established. However, the evidence is indirect, based on the observations of the glasses quenched from the liquid. Levitation techniques, with both wide- and small-angle diffraction, should permit *in situ* observation of the coexistence of two such states in the liquid.

The experience gained in the present work should be extended to other structural measurements, for example wide- and small-angle neutron scattering. A neutron diffraction measurement of liquid Al_2O_3 has reportedly been performed at the ISIS pulsed spallation neutron source in the UK [87]. This opens up the possibility of exploiting the generally different contrast between neutron and x-ray scattering to derive information about complex systems at the partial level. Anomalous x-ray scattering and neutron diffraction with isotope substitution should also be exploited for these purposes. In addition, one can expect that quasielastic neutron scattering and inelastic x-ray scattering will be used to obtain dynamical information about stable and metastable liquids at high temperature.

Finally, we can expect that structural information of the type reviewed in this article will be correlated with an expanded range of measurements of physical and chemical properties. Examples include the simultaneous measurement of conductivity and magnetic permeability with contactless methods [88], use of modern solid-state NMR to investigate metastable solid phases, and optical techniques such as UV Raman scattering and photon correlation spectroscopy.

Acknowledgments

This work was supported by the US Department of Energy SBIR contract number DE-FG02-94ER81732 and by the Division of Materials Sciences, Office of Basic Energy Sciences, under contract W-31-109-ENG-38. The authors thank Drs Lonnie Berman, P A Montano and M A Beno for making the experiments at NSLS possible, Drs J A Odriozola and M Wilson for providing MD results and Drs I Egry and C Landron for providing advance copies of their manuscripts. Special thanks are due to Dr S Ansell of ESRF for development of the data analysis algorithms, and to Drs Paul Nordine and Marie-Louise Saboungi for their support of the work and valuable discussions. The National Synchrotron Light Source at Brookhaven National Laboratory is supported by the Divisions of Materials Sciences and Chemical Sciences of the DOE.

References

[1] Aasland S and McMillan P F 1994 *Nature* **369** 633
[2] Poole P H, Grande T, Angell C A and McMillan P F 1997 *Science* **275** 322
[3] Platzek D, Notthoff C, Herlach D M, Jacobs G, Herlach D and Maier K 1994 *Appl. Phys. Lett.* **65** 1723
[4] Weber J K R 1997 *Eur. J. Solid State Inorg. Chem.* **34** 847
[5] Weber J K R, Felten J J, Cho B and Nordine P C 1998 *Nature* **393** 769
[6] Weber J K R, Krishnan S and Nordine P C 1991 *JOM Mag.* **43** 8
[7] Muck O 1923 *German Patent* 42204
[8] Winborne D A, Nordine P C, Rosner D E and Marley N F 1976 *Metall. Trans.* B **7** 711
[9] Coutures J P, Massiot D, Bessada C, Echegut P, Rifflet J C and Taulelle F 1990 *C. R. Acad. Sci. Paris.* **310** 1041
[10] Bolsaitis P, Spjut R E and Elliot J F 1989 *High Temp. High Pressures* **21** 601
[11] Weber J K R, Hampton D S, Merkley D R, Rey C A, Zatarski M M and Nordine P C1994 *Rev. Sci. Instrum.* **65** 456
[12] Ansell S, Krishnan S, Felten J J and Price D L 1998 *J. Phys.: Condens. Matter* **10** L73
[13] Ansell S, Krishnan S, Weber J K R, Felten J J, Nordine P C, Beno M A, Price D L and Saboungi M-L 1997 *Phys. Rev. Lett.* **78** 464
[14] Krishnan S, Ansell S, Felten S, Volin K J and Price D L 1998 *Phys. Rev. Lett.* **81** 576
[15] Krishnan S, Ansell S and Price D L 1998 *J. Am. Ceram. Soc.* **81** 1967
[16] Ansell S, Krishnan S and Price D L 1999 *Computer-Aided Design of High Temperature Materials* ed A Pechenik, A K Kalia and P Vashishta (New York: Oxford University Press) pp 34–46
[17] Krishnan S, Ansell S and Price D L 1999 *J. Non-Cryst. Solids* **250–252** 286
[18] Weber J K R, Krishnan S, Ansell S, Hixson A and Nordine P C 2000 *Phys. Rev. Lett.* at press
[19] Landron C, Hennet L, Berthet P, Coutures J-P and Berar J-F 1999 *Japan. J. Appl. Phys.* **38** 87
[20] Landron C, Launay X, Rifflet J C, Echegut P, Auger Y, Ruffier D, Coutures J-P, Lemonier M, Gailhanou M, Bessiere M, Bazin D and Dexpert H 1997 *Nucl. Instrum. Methods Phys. Res.* B **124** 627
[21] Landron C, Hennet L, Coutures J-P, Gailhanou M, Gramond M and Berar J F 1998 *Europhys. Lett.* **44** 429
[22] Jacobs G, Egry I, Maier K, Platzek D, Reske J and Frahm R 1996 *Rev. Sci. Instrum.* **67** 3683
[23] Egry I, Lohofer G, Gorges E and Jacobs G 1996 *J. Phys.: Condens. Matter* **8** 9363
[24] Jacobs G, Egry I, Gorges E and Langen M 1998 *Int. J. Thermophys.* **19** 895
[25] Jacobs G and Egry I 1999 *Phys. Rev.* B **59** 3961
[26] Krishnan S, Felten J J, Rix J E, Weber J K R, Nordine P C, Ansell S, Beno M A and Price D L 1997 *Rev. Sci. Instrum.* **68** 3512
[27] Weber J K R and Nordine P C 1995 *Microgravity Sci. Technol.* **7** 279
[28] Krishnan S, Weber J K R, Schiffman R A and Nordine P C 1991 *J. Am. Ceram. Soc.* **74** 881
[29] Krishnan S, Weber J K R, Nordine P C, Schiffman R A, Hauge R H and Margrave J L 1991 *High Temp. Sci.* **30** 137
[30] Krishnan S and Nordine P C 1996 *J. Appl. Phys.* **80** 1735
[31] Krishnan S, Yugawa K J and Nordine P C 1997 *Phys. Rev.* B **55** 8201
[32] Cezairliyan A and Miiller A P 1984 *Int. J. Thermophys.* **5** 315
[33] Baro J, Roteta M, Fernandez-Varea J M and Salvat F 1994 *Radiat. Phys. Chem.* **44** 531
[34] Chihara J 1987 *J. Phys. F: Met. Phys.* **17** 295
[35] Soper A K 1989 *Inst. Phys. Conf. Proc. R. Soc.* **97** 711

[36] Sanz J F, Capitan M J and Odriozola J A 1995 *J. Phys. Chem.* **99** 17 872
[37] Coutures J-P, Massiot D, Bessada D, Echegut P, Rifflet J C and Taulelle F 1990 *C. R. Acad. Sci. Paris.* **310** 1041
[38] Price D L, Moss S C, Reijers R, Saboungi M-L and Susman S 1988 *J. Phys. C: Solid State Phys.* **21** L1069
[39] Shannon R D and Prewitt C T 1969 *Acta. Crystallogr.* B **25** 925
[40] Meade C, Hemly R J and Mao H K 1992 *Phys. Rev. Lett.* **69** 1387
[41] Sato R K, McMillan P F, Dennison P and Dupree R 1991 *J. Phys. Chem.* **95** 4483
[42] Levi C G, Jayaram V, Valencia J J and Mehrabian R 1988 *J. Mater. Res.* **3** 969
[43] Weber J K R, Anderson C D, Merkley D R and Nordine P C 1995 *J. Am. Ceram. Soc.* **78** 577
[44] Navrotsky A 1994 *Physics and Chemistry of Earth Materials* (New York: Cambridge University Press)
[45] San Miguel M A, Sanz J F, Alvarez L J and Odriozola J A 1998 *Phys. Rev.* B **58** 2369
[46] Hemmati M, Wilson M and Madden P A 1999 *J. Phys. Chem.* B **103** 4023
[47] Lamparter P and Kniep R 1997 *Physica* B **234–236** 405
[48] Enderby J E, Ansell S, Krishnan S, Price D L and Saboungi M-L 1997 *Appl. Phys. Lett.* **71** 116
[49] Massalski T B, Murray J L, Bennett L H and Baker H 1986 *Binary Alloy Phase Diagrams* (Metals Park, OH: American Society of Metals) p 1799
[50] Anderson R C 1980 *High Temperature Oxides* ed A M Alper (New York: Academic) pp 1–37
[51] Pettifor D G 1986 *J. Phys. C: Solid State Phys.* **19** 285
[52] Tosi M P, Price D L and Saboungi M-L 1993 *Annu. Rev. Phys. Chem.* **44** 173
[53] Alvarez L, San Miguel M A and Odriozola J A 1999 *Phys. Rev.* B **59** 11 303
[54] Saboungi M-L, Price D L, Scamehorn C and Tosi M P 1991 *Europhys. Lett.* **15** 283
[55] Naslain R 1977 *Boron and Refractory Borides* ed V I Matkovich (New York: Springer) 139–203
[56] Buschbeck K C 1981 *Boron Compounds, Elemental Boron, and Boron Carbides (Gmelin Handbook of Inorganic Chemistry 13)* (Berlin: Springer)
[57] Delplane R G, Lundstrom T, Dahlborg U and Howells W S 1991 *Boron-Rich Solids (AIP Conf. Proc. 231)* ed D Emin, T L Aselage, A C Switendick and C L Beckel (New York: AIP) p 241
[58] Vast N, Bernard S and Zerah G 1995 *Phys. Rev.* B **52** 4123
[59] Galli G and Gygi F 1998 *Bull. Am. Phys. Soc.* **43** 318
[60] Galli G and Parinello M 1991 *J. Chem. Phys.* **95** 7504
[61] Khantadze D V and Topuridze N J 1986 *J. Less Common Met.* **117** 105
[62] Sasaki H, Tokizaki E, Terashima K and Kimura S 1994 *Japan. J. Appl. Phys.* **33** 3803
[63] Rhim W-K, Chung S K, Rulison A J and Spjut R E 1997 *Int. J. Thermophys.* **18** 459
[64] Glazov V M, Chizhevskaya S N and Glagoleva N 1969 *Liquid Semiconductor* (New York: Plenum)
[65] Sasaki H, Tokisaki E, Huang X-M, Terashima K and Kimura S 1995 *Japan. J. Appl. Phys.* **34** 3432
[66] Sasaki H, Ikari A, Terashima K and Kimura S 1995 *Japan. J. Appl. Phys.* **34** 3426
[67] Schnyders H S and Van Zytfeld J B 1996 *J. Phys.: Condens. Matter* **8** 10 875
[68] Grabow M H and Gilmer G H 1989 *Mater. Res. Soc. Symp. Proc.* vol 141 (Pittsburgh, PA: Materials Research Society) p 341
[69] Jank W and Hafner J 1990 *Phys. Rev.* B **41** 1497
[70] Stich I, Car I and Parinello M 1989 *Phys. Rev. Lett.* **76** 2077
[71] Stich I, Car R and Parinello M 1989 *Phys. Rev.* B **44** 4262
[72] Stich I, Parinello M and Holender J M 1996 *Phys. Rev. Lett.* **76** 2077
[73] Waseda Y, Shinoda K, Sugiyama K and Takeda S 1995 *Japan. J. Appl. Phys.* **34** 4124
[74] Kita Y, Van Zytfeld J B, Morita Z and Iida T 1994 *J. Phys.: Condens. Matter* **6** 811
[75] Ludke W D and Landman U 1988 *Phys. Rev.* B **37** 4656
[76] Angell C A, Borick S S and Grabow M H 1996 *J. Non-Cryst. Solids* **205–207** 463
[77] Angell C A and Borick S S 1999 *J. Phys.: Condens. Matter* **11** 8163
[78] Donovan E P, Spaepan F, Turnbull D, Poate J M, and Jacobson D C 1985 *J. Appl. Phys.* **57** 1795
[79] Waseda Y 1980 *The Structure of Non-Crystalline Materials* (New York: McGraw-Hill)
[80] Wilde G, Gorler G P and Willnecker R 1996 *Appl. Phys. Lett.* **68** 2953
[81] Reske J, Herlach D M, Keuser F, Maier K and Platzek D 1995 *Phys. Rev. Lett.* **75** 737
[82] Herlach D M, Holland-Moritz D, Schenk T, Schneider K and Wilde G 1999 *J. Non. Cryst. Solids* **250–252** 286
[83] Volkmann T, Wilde G, Willnecker R and Herlach D M 1998 *J. Appl. Phys.* **83** 3028
[84] Eder O J, Erdpresser E, Kunsch B, Stiller H and Suda M 1980 *J. Phys. F: Met. Phys.* **10** 83
[85] Waseda Y and Ohtani M 1974 *Phys. Status Solidi* **62** 535
[86] Eder O J, Erdpresser E, Kunsch B, Stiller H and Suda M 1980 *J. Phys. F: Met. Phys.* **10** 183
[87] Landron C and Soper A K 1999 private communication
[88] Schnyders H, Enderby J E and Saboungi M-L 1999 *Appl. Phys. Lett.* **20** 3213